



# A tool for estimating ground-based InSAR acquisition characteristics prior to monitoring installation and survey and its differences from satellite InSAR

Charlotte Wolff<sup>1</sup>, Marc-Henri Derron<sup>1</sup>, Carlo Rivolta<sup>2</sup>, and Michel Jaboyedoff<sup>1</sup>

<sup>1</sup>ISTE, University of Lausanne, 1015 Lausanne, Switzerland

<sup>2</sup>Ellegi srl, 20123 Milan, Italy

**Correspondence:** Charlotte Wolff ([charlotte.wolff@unil.ch](mailto:charlotte.wolff@unil.ch))

Received: 3 November 2023 – Discussion started: 21 November 2023

Revised: 11 June 2024 – Accepted: 18 June 2024 – Published: 29 July 2024

**Abstract.** Synthetic Aperture Radar (SAR) acquisition can be performed from satellites or from the ground by means of a so-called GB-InSAR (Ground-Based Interferometry SAR), but the signal emission and the output image geometry slightly differ between the two acquisition modes. Those differences are rarely mentioned in the literature. This paper proposes to compare satellite and GB-InSAR in terms of (1) acquisition characteristics and parameters to consider; (2) SAR image resolution; and (3) geometric distortions that are foreshortening, layover, and shadowing.

If in the case of satellite SAR, the range and azimuth resolutions are known and constant along the orbit path, in the case of GB-InSAR their values are terrain-dependent. It is worth estimating the results of a GB-InSAR acquisition that one can expect in terms of range and azimuth resolution, line of sight (LoS) distance, and geometric distortions to select the best installation location when several are possible. We developed a novel tool which estimates those parameters from a digital elevation model (DEM), knowing the GB-InSAR and the slope of interest (SoI) coordinates. This tool, written in MATLAB, was tested on a simple synthetic point cloud representing a cliff with a progressive slope angle to highlight the influence of the SoI geometry on the acquisition characteristics and on two real cases of cliffs located in Switzerland, namely one in the Ticino canton and one in the Vaud canton.

## 1 Introduction

The use of Synthetic Aperture Radar Interferometry (InSAR) as a remote-sensing technique capable of detecting and monitoring small ground displacements started in the 1980s (Gabriel et al., 1989). It was initially used specifically with spaceborne platforms such as the satellites ERS-1 (1991) or RADARSAT (1995; Zebker and Villasenor, 1992; Massonet et al., 1993; Usai and Hanssen, 1997). In the field of geosciences, this technique has been primarily dedicated to studying small movement phenomena (smaller than a few centimetres) across large areas (km) with a resolution ranging from decametric to metric scales, such as subsidence (Cabral-Cano et al., 2008; Strozzi et al., 2018), volcanic activities (Wicks et al., 1998; Garthwaite et al., 2019), or landslides (Tarchi, 2003; Hilley et al., 2004; Colesanti and Wasowski, 2006). Since then, the technique expanded, and by the late 1990s, the first radar devices monitoring displacements from a ground base (GB) were deployed (Cazzanil et al., 2000; Pieraccini and Miccinesi, 2019; Tarchi et al., 1997). Some use a Real Aperture Radar (RAR) antenna (Werner et al., 2008), while others employ a Synthetic Aperture Radar (SAR, Rudolf et al., 1999; Leva et al., 2003; Antonello et al., 2003).

InSAR satellites and GB-InSAR are complementary, with both detecting displacements only along their respective line of sight (LoS) (Casagli et al., 2003; Catani et al., 2014; Carlà et al., 2019). InSAR satellites detect sub-vertical movements, while GB-InSAR devices gather information on sub-horizontal movements (Wolff et al., 2023).

Radar image acquisition and processing are sensitive to terrain geometry, which can have significant effects on the appearance of the resulting radar image, such as slope compression and highlighting (foreshortening and layover effects) (Jensen, 2006) or surfaces not illuminated by the radar appearing dark and elongated in the image (shadowing effect). Terrain slopes and the radar incidence angle influence the image resolution. Satellite-imagery-oriented software creates foreshortening and layover masks (Kropatsch and Strobl, 1990; Rees, 2000). Although SAR satellite geometries are well documented (Griffiths, 1995; Rees, 2000; McCandless and Jackson, 2004; Ferretti et al., 2007), the transposition of these geometries to GB-InSAR is seldom mentioned in the literature. Nevertheless, before initiating a new GB-InSAR campaign, it is crucial to estimate what results one can expect in terms of the distance to the region of interest, range, and azimuthal resolutions, as well as potential foreshortening and shadowing effects, in order to select the best position before starting the campaign. This is particularly the case for the installation of a GB-InSAR in remote areas and difficult installation sites (Lingua et al., 2008; Caduff et al., 2015; Talich, 2016; Rouyet et al., 2017).

After transposing the SAR geometry described for satellites to ground SAR geometry and presenting the main differences between satellite and GB-InSAR, this paper describes a MATLAB tool with a user interface designed to compute several parameters of the radar image such as its range and azimuthal resolutions, as well as the areas affected by shadowing or strong foreshortening in the case of a linear SAR system consisting of a radar measuring head moving along a rail. The needed inputs are a digital elevation model (DEM) in an ASCII format, the localization of the area of interest, and the localization where one intends to install the GB-InSAR. The main objective is to provide a tool for helping surveyors to find the best installation location.

The tool has been tested across three study cases: (1) a synthetic cliff made of slope angles increasing from the bottom to the top and two real, unstable cliffs that have been monitored with a GB-InSAR at (2) Cima del Simano and (3) La Cornalle. For Cima del Simano, the results for three different radar positions were compared to select the best installation position.

## 2 Theory

### 2.1 SAR geometry

The geometrical characteristics of radar imagery differ from standard image geometry (Lin and Fuh, 1998; Turner et al., 2021). In the case of radar imagery, some parameters need to be defined and distinguished when applied to satellite and aerial InSAR or to GB-InSAR. The abbreviations are summarized in Table 1.

#### 2.1.1 LoS, azimuthal, and range directions

In the case of aerial radar, the azimuthal direction corresponds to the direction of the displacement of the aircraft or satellite; the range direction, or look direction, is the direction perpendicular to the azimuthal direction. The direction of the radar-to-target line is the LoS direction whose distance is called the range or LoS distance (dLoS). It varies from near-range, for the line forming the smaller angle with the vertical radar–Earth line (nadir), to the far-range for the direction with the larger angle (Fig. 1a).

In the case of the GB-InSAR, the azimuthal and range directions are parallel and perpendicular to the rail, respectively. The dLoS definition is similar to the aerial radar case, but the near-range is the line forming the smaller angle with the horizontal line, and the far-range is the larger angle (Fig. 1b).

#### 2.1.2 Look angle or off-nadir angle $\Phi$ , incident angle $\theta$ , and depression angle $\gamma$

Look angle or off-nadir angle  $\Phi$ , incident angle  $\theta$ , and depression angle  $\gamma$  are well defined in the case of satellite imagery when the monitored surface is assumed to be sub-horizontal. The look angle  $\Phi$  is the angle between the vertical line and the LoS. The depression angle  $\gamma$  is the complementary angle of the look angle. The definition of the incident angle  $\theta$  is the same as in optical geometry, i.e. the angle between the LoS and the normal to the monitored surface (Fig. 2a and b). To simplify, when the monitored surface is horizontal for satellite InSAR or vertical for GB-InSAR, both  $\theta$  and  $\Phi$  are the angles between the LoS and the normal to the observed surface and are thus assumed to be equal.

#### 2.1.3 Antenna beamwidth $\varepsilon$

The emitted signal propagates within a certain emission cone defined by an angle called beamwidth  $\varepsilon$  (Miron, 2006; Woodhouse, 2006), which is proportional to the wavelength according to diffraction laws (Lipson et al., 1995) and defines the maximum extent of the illuminated area. The radar footprint on the ground is an ellipsoid (Fig. 1a and b). Radar manufacturers provide antenna emission characteristics that are displayed in the form of a polar diagram (Toomay and Hannen, 2004). In the case of GB-InSAR, the vertical beamwidth  $\varepsilon_v$  is limited to  $30^\circ$  to avoid interferences with other radar devices such as planes (Anon, 2017; ETSI EN 300 440 v2.1.1), while the horizontal beamwidth  $\varepsilon_h$  is not legislatively restricted (Fig. 1d).

#### 2.1.4 Radar bandwidth BW, satellite radar pulse length $\tau_{\text{FMPR}}$ , and GB-InSAR sweep length $\tau_{\text{MPCW}}$

One of the major differences between GB-InSAR and satellite InSAR is related to their emitted signal. In the case of

**Table 1.** List of abbreviations used for the radar characteristics presented hereafter.

Name	Abbreviation	Unit	Definition
Line-of-sight vector	<i>LoS</i>	m	Vector between radar and target points
LoS distance	dLoS	m	Radar to target distance
Distance on slope	$D_{\text{slope}}$	m	Distance of illuminated surface along the slope in the range direction
Look or nadir angle	$\Phi$	$^{\circ}$	Angle between the vertical line and the LoS
Incident angle	$\theta$	$^{\circ}$	Angle between LoS and the normal of the targeted surface
Depression angle	$\gamma$	$^{\circ}$	Complement angle to $\Phi$
Apparent orientation	$\omega$	$^{\circ}$	Horizontal angle between LoS and target slope strike
Slope dip	$\alpha$	$^{\circ}$	Slope dip
Apparent slope dip	$\alpha_{\text{app}}$	$^{\circ}$	Apparent slope dip seen from radar position
Speed of light	$c$	$\text{m s}^{-1}$	$3 \times 10^8$
Radar wavelength	$\lambda$	cm	Spatial period of the signal
Frequency	$f$	GHz	$f = c/\lambda$
Frequency-modulated pulsed radar	FMPR	–	Type of radar to which satellite InSAR belongs (Mahafza, 2000; Nadav, 2003)
Frequency-modulated continuous wave	FMCW	–	Type of radar to which GB-InSAR belongs (Wolff, 1998; Nadav, 2003)
Pulse length	$\tau_{\text{FMPR}}$	$\mu\text{s}$	In the case of satellite InSAR, duration of the emission of the emission of one radar pulse
Sweep length	$\tau_{\text{FMCW}}$	$\mu\text{s}$	In the case of GB-InSAR, duration of one sequence of frequency variation
Pulse repetition interval	PRI	$\mu\text{s}$	In the case of satellite InSAR, it is the time between the emission of two consecutive radar pulses
Pulse repetition frequency	PRF	MHz	$\text{PRF} = 1/\tau_{\text{FMPR}}$
Frequency bandwidth	BW	MHz	Difference between the upper and lower cut-off frequencies: for satellite InSAR it is $\text{BW} = 1/\tau_{\text{FMPR}}$ (Mahafza, 2000); for GB-InSAR it is $\text{BW} = 1/\tau_{\text{FMCW}}$
Antenna beamwidth	$\varepsilon$	$^{\circ}$	Angle from which the majority of the antenna's power radiates  In the case of GB-InSAR, the vertical and horizontal beamwidths are different and denoted $\varepsilon_v$ and $\varepsilon_h$
Illuminated area length	$W_{\text{illu}}$	m	Length of the illuminated area in the case of the GB-InSAR, which increases with the range
Illuminated area height	$H_{\text{illu}}$	m	Height of the illuminated area in the case of the GB-InSAR
Synthetic antenna length	$L$	m	In the case of linear GB-InSAR, rail length used to focus the radar image (which is shorter than the total rail length) $L$ is generally 2 or 3 m In the case of satellite InSAR, $L$ can be several kilometres.
Real antenna length	$L_{\text{real}}$		In the case of satellite InSAR, radar antenna length
Resolution	$R$	m	Size of the smallest object detectable by the sensor
Ground range resolution	$R_r$	m	Resolution (ground pixel size) of the radar image along the line of sight
Azimuthal resolution	$R_{\text{az}}$	m	Resolution (ground pixel size) of the radar image along the line parallel to the sensor's motion

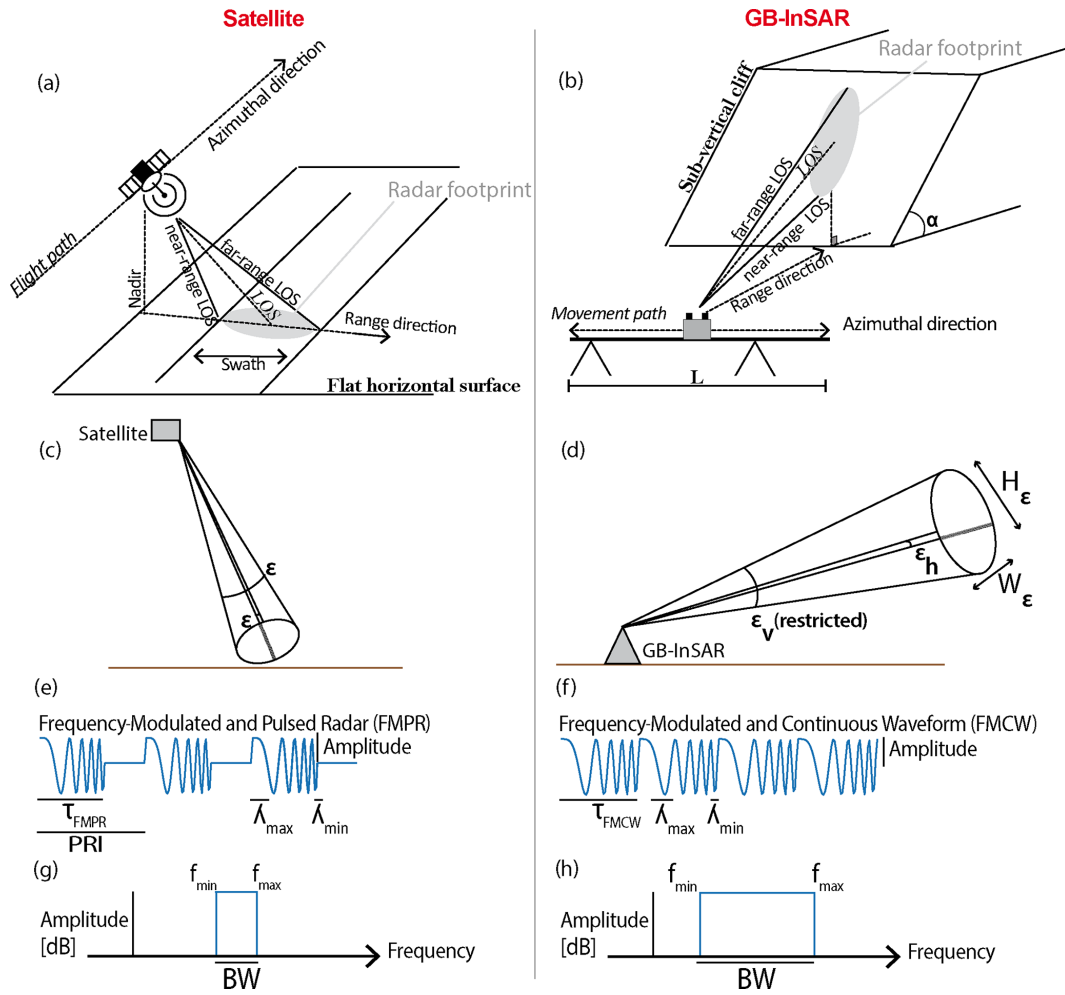


**Figure 1.** Illustration and comparison of radar acquisition characteristics in the case of satellite InSAR (a, c, e, g) and GB-InSAR (b, d, f, h). (a, b) Geometry of the acquisition defining the azimuthal and range directions. (c, d) Beamwidth characteristics. (e, f) Waveform characteristics. (g, h) Frequency characteristics.

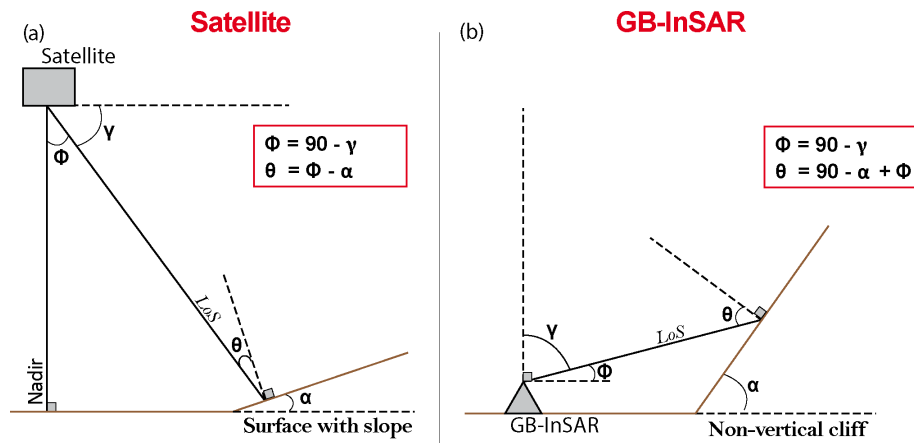


**Figure 2.** Illustration of the main specific angles used when describing a SAR acquisition. (a) Case of satellite radar acquisition. (b) Case of GB-InSAR acquisition.

satellite InSAR, the transmitted signal must have sufficient amplitude to reach the Earth's surface and be backscattered with enough intensity to be detected by the radar receiver (Ferretti et al., 2014). However, the antennas are not able to continuously generate and send such a high-peak power signal. To overcome this technical limitation, the satellite radar signal is sent by pulses defined by a certain pulse duration  $\tau_{\text{FMPR}}$  comprising between 10 and 100  $\mu\text{s}$ , depending on the satellite (Fig. 1d). The emitted signal frequency is modulated to perform a pulse compression or chirping (Hein, 2004; Klauder et al., 1960). Such a radar can be named frequency-modulated pulsed radar (FMPR). The satellite radar bandwidth (BW; Fig. 1g) is the difference between the maximal and minimal emitted frequency. The time between two consecutive pulses is called the pulse repetition interval (PRI), and the duration of the emission of one pulse is the pulse length  $\tau_{\text{FMPR}}$ .

The European Telecommunications Standards Institute (ETSI) defined some standards regarding the short-range devices (SRDs) emitting radio signals (Anon, 2017). The power and the frequencies of signals sent by terrestrial radar are limited to not interfere with other devices emitting and receiving radio signals. Specifically, for GB-InSAR operating in the frequency range of 17.1 to 17.3 GHz, the maximum limits for the frequency bandwidth and the power output are 200 MHz and 26 dBm, respectively.

GB-InSAR is considered a frequency-modulated continuous wave radar (FMCW radar; Wolff, 1998; Nadav, 2003), the signal emitted is of a lower intensity compared to satellite radar emissions. Since the signal is continuously emitted, one is lacking the timing necessary to isolate the backscattered signals and discriminate the range. This is achieved instead by modulating the frequency sent by the transmitter (Fig. 1f). The GB-InSAR bandwidth (BW; Fig. 1h) is the difference between the upper and lower cut-off frequencies. The duration of one sequence of frequency variation is the sweep length  $\tau_{\text{FMCW}}$ .

BW, in the case of satellites, is generally smaller than for GB-InSAR, ranging between 10 and 80 MHz and between 70 and 200 MHz, respectively.

### 2.1.5 Real antenna length $L_{\text{real}}$ and synthetic antenna length $L$

The azimuthal resolution is inversely proportional to the real antenna length  $L_{\text{real}}$  for RAR acquisition. In the case of SAR acquisition, a synthetic aperture antenna  $L$  is used to increase this resolution. For a GB-InSAR installed on a rail, the antenna length  $L$  corresponds to the rail length used to focus the radar image, which is in practice slightly shorter than the total rail length.

## 2.2 Spatial resolution

### 2.2.1 Radar and optical images

When representing the world (Fig. 3a and d) in an image, one must distinguish the radar image from the optical image, which is the visual display we are commonly used to seeing (Fig. 3b). The radar image is based on the distance between the radar antenna and each feature of the scene; the bottom line of the image corresponds to the monitored surface closest to the radar. Additionally, in radar geometry, range and azimuthal resolutions are defined differently, and by default, pixels are not square (Fig. 3c and e).

### 2.2.2 Azimuthal resolution $R_{\text{az}}$

The azimuthal resolution  $R_{\text{az}}$  corresponds to the resolution parallel to the flying trajectory in the case of satellite InSAR or parallel to the rail in the case of a linear GB-InSAR or to the horizontal resolution in the radar image. Its value differs between satellite InSAR and GB-InSAR.

The synthetic antenna aperture length being constrained by the rail length for the GB-InSAR,  $R_{\text{az}}$ , is related to the radar beamwidth (itself related to the wavelength  $\lambda$ ), the range distance dLoS, and the synthetic antenna length  $L$  with the following relation (Henderson and Lewis, 1998; Jensen, 2006):

$$R_{\text{az,GB-InSAR}} = \frac{d\text{LoS}\lambda}{2L}. \quad (1)$$

Thus,  $R_{\text{az}}$  increases from the near- to far-range and the GB-InSAR image of a slope is a cone (Fig. 3d). Conversely, for the satellite, the synthetic aperture length  $L$  can be infinite, and  $R_{\text{az}}$  is dLoS-free and  $\lambda$ -free (Henderson and Lewis, 1998) and defined as follows:

$$R_{\text{az,satellite}} = \frac{L_{\text{real}}}{2}. \quad (2)$$

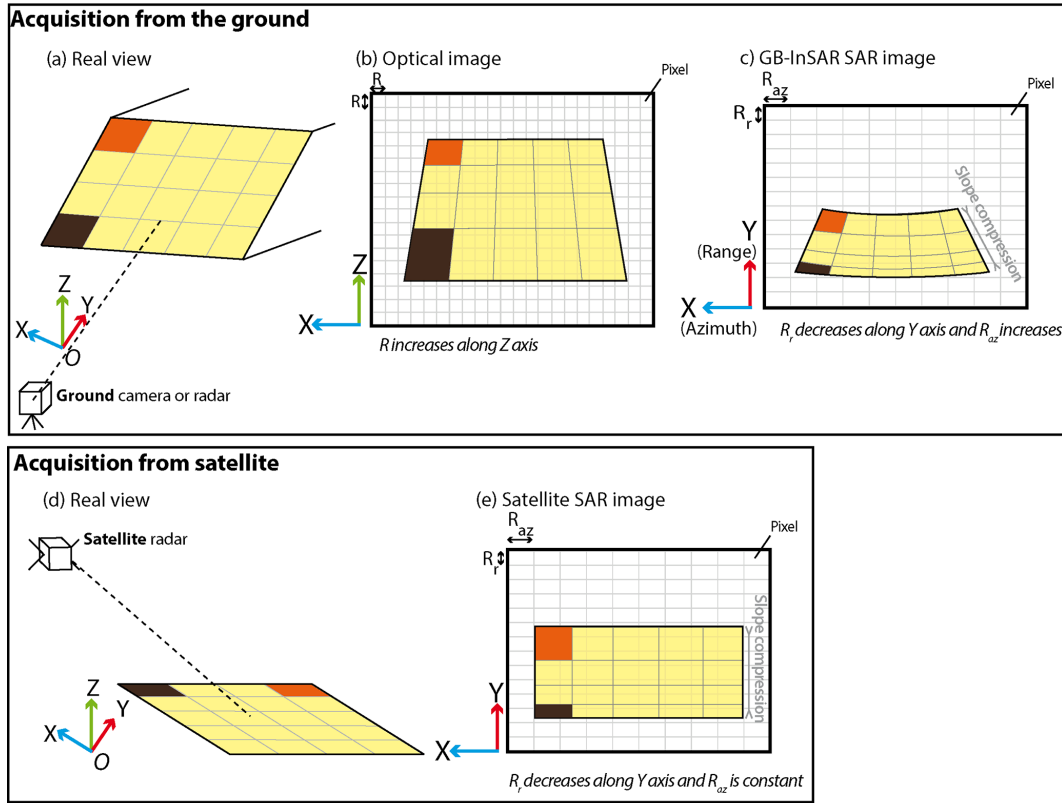
The satellite InSAR image of a slope is thus rectangular (Fig. 3c).

Figure 4 presents the influence of dLoS and  $L$  on the azimuthal resolution in the case of the GB-InSAR.

### 2.2.3 Ground range resolution $R_{\text{r}}$

The ground range resolution  $R_{\text{r}}$  is the resolution along the LoS direction or the vertical resolution. It corresponds to the minimum time needed to distinguish two consecutive pulses (Woodhouse, 2006). It is ground-geometry-dependent and linked to the incidence angle  $\theta$ , the speed of light  $c$ , and the pulse length  $\tau_{\text{FMPR}}$  (after pulse compression) or sweep length  $\tau_{\text{FMCW}}$ , according to the following relations (Henderson and Lewis, 1998; Jensen, 2006; Mahafza, 2000; McCandless and Jackson, 2004):

$$R_{\text{r,satellite}} = \frac{\tau_{\text{FMPR}}c}{2\sin\theta} = \frac{c}{2\text{BW}\sin\theta} = \frac{c}{2\text{BW}\sin(\Phi - \alpha_{\text{app}})}. \quad (3)$$



**Figure 3.** Comparison of the view of a surface area. (a) Real view in a parallel projection with the camera or radar acquiring the image from the ground. (b) Optical image taken with a camera from the ground.  $R$  increases with  $Z$ . Consequently, the distance between two consecutive horizontal lines decreases along  $Z$ . (c) GB-InSAR SAR image (after Tapete et al., 2013).  $R_{az}$  increases, and  $R_r$  decreases along  $Y$ . Consequently, the distance between two consecutive horizontal lines increases along  $Z$ . (d) Real view in a parallel projection with the satellite radar acquiring the image from the satellite orbit. (e) Satellite SAR image.  $R_{az}$  is constant along  $Y$ , while  $R_r$  decreases. Consequently, the distance between two consecutive horizontal lines increases along  $Y$ . In the case of the radar images (c, e), the slope is compressed compared to the optical image due to the foreshortening effect.

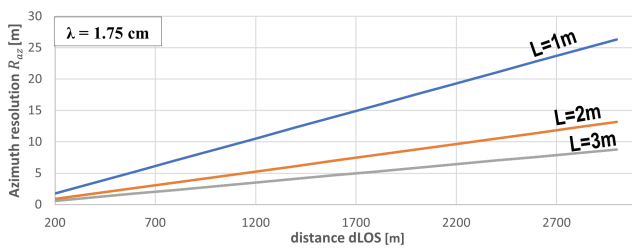


**Figure 4.** Influence of the rail length used to focus the GB-InSAR image corresponding to the synthetic antenna length  $L$  and the distance  $dLoS$  on the azimuthal resolution  $R_{az}$  for a Ku band with a wavelength equal to  $\lambda = 1.75$  cm. The longer the rail length, the better the azimuthal resolution will be.

$$\begin{aligned}
 R_{r,GB-InSAR} &= \frac{\tau_{FMCW}c}{2 \sin \theta} = \frac{c}{2BW \sin \theta} \\
 &= \frac{c}{2BW \sin (90 - \alpha_{app} + \Phi)} \\
 &= \frac{c}{2BW \cos (\Phi - \alpha_{app})}.
 \end{aligned}
 \tag{4}$$

The monitored cliff geometry has an impact on the range resolution with two major consequences, according to Eq. (4): (1) near-range surfaces and features possess, along a planar topography, less resolution in range than those in the far-range because  $\Phi$  increases with the range, and (2) steeper slopes increase the range resolution by increasing  $\alpha_{app}$  (Fig. 5; Sabins, 1997; Stimson, 1998; Jensen, 2006). Furthermore, the shorter the pulse length  $\tau_{FMPR}$  or sweep length  $\tau_{FMCW}$ , the finer the resolution will be. Nevertheless, one must be careful with the choice of the pulse length because if a short  $\tau_{FMPR}$  or  $\tau_{FMCW}$  results in a better resolution, then the backscatter signal is also weaker and might not be detected if too low. For GB-InSAR, the parameter that can be chosen by the user is the bandwidth (BW). The further away the radar is installed from the target area, the smaller the bandwidth should be to be sure to detect the backscattered signal. A good balance between an acceptable resolution and a sufficiently strong backscattered signal must be found (Fig. 6a and b).

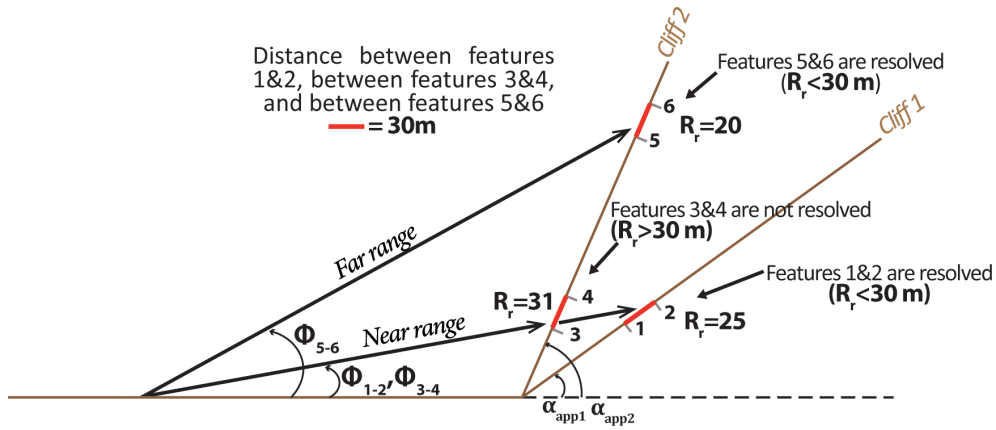


**Figure 5.** Ground range resolution  $R_r$  for two different slope angles and two different depression angles (adapted from Sabins, 1997). The distance between features 1 and 2, features 3 and 4, and features 5 and 6 is the same at 30 cm. However, features 1 and 2, located on a gentle slope and at a near-range distance from the GB-InSAR, are resolved ( $R_r = 25$  m); features 5 and 6 are located at a far-range distance on a steep slope and are also resolved ( $R_r = 20$  m), while features 3 and 4 are located on the same steep slope as features 5 and 6 but at a near-range distance and are not resolved ( $R_r = 31$  m).

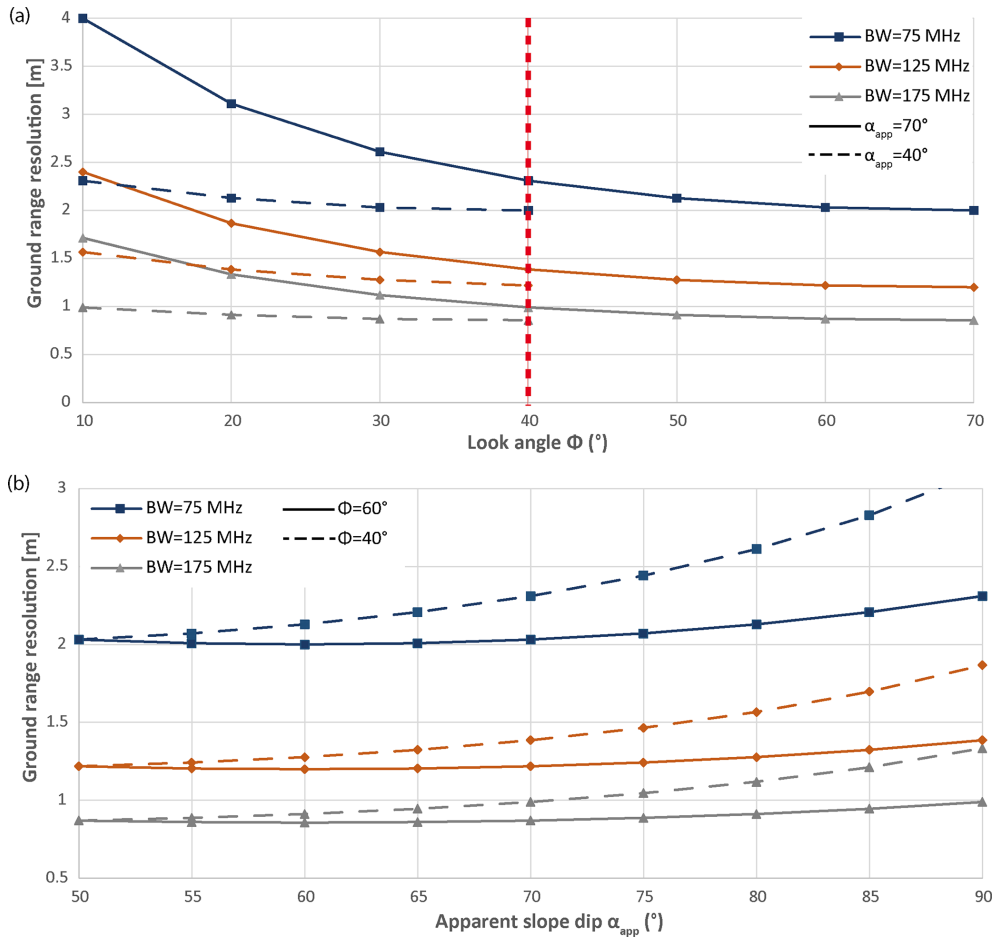


**Figure 6.** Influence of some GB-InSAR parameters on the range resolution  $R_r$ . (a) Influence of the look angle  $\Phi$  for different BWs. It is interesting to notice that the resolution varies a little when  $\Phi$  is larger than  $40^\circ$ . (b) Influence of the apparent slope dip  $\alpha_{app}$  for different BWs.

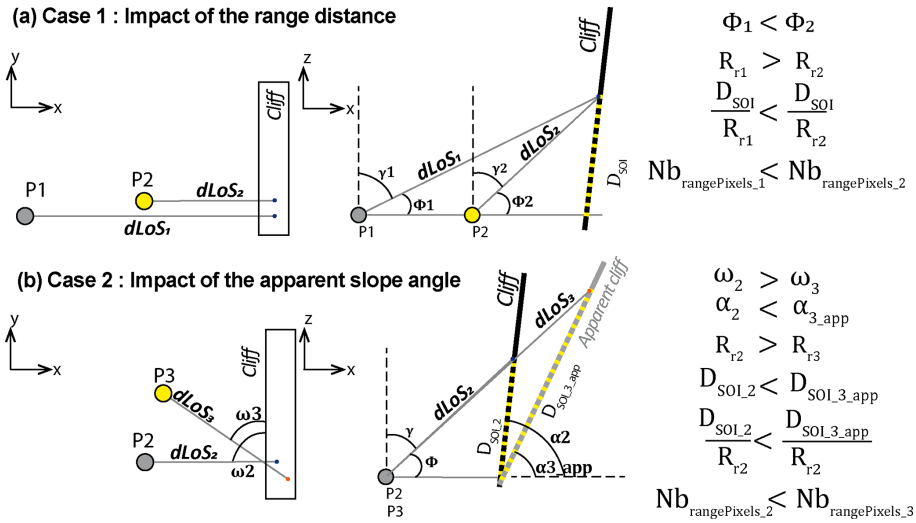


**Figure 7.** Two scenarios of the selection of the best GB-InSAR installation to get the lower compression of the SoI in range. The best location is highlighted in yellow. **(a)** Case 1 shows the installation near vs. far from the monitored cliff. **(b)** Case 2 shows the installation in front of vs. aside the monitored cliff. When looking from the aside position,  $\alpha_{app}$  is smaller according to Eq. (6), and the apparent SoI length on slope in the radar direction is longer so the information is distributed across more pixels within the range distance.

**2.2.4 Number of pixels and slope compression**

During a monitoring campaign, the surveyor focuses on a slope of interest (SoI). A monitoring campaign is effective when information concerning this SoI is distributed across a wide range of pixels rather than compressed within a few; this involves attempting to get the finest possible range resolution. The position of the GB-InSAR will have an influence on the resolution, and the number of pixels in which the SoI will be contained can be estimated with the following formula:

$$Nb_{pixelRange} = \frac{D_{SoI}}{R_r}, \tag{5}$$

where  $D_{SoI}$  is the distance along the monitored slope of the SoI.

The steeper the slope, the more the information will be compressed, and some interesting features may be contained in the same pixel. Given this consideration, if one has the choice between two radar installations, it is worth (1) reducing the range distance (Fig. 7a) and (2) reducing the apparent slope angle  $\alpha_{app}$  of the measured cliff to increase the apparent SoI distance (Fig. 7b). The apparent slope angle can be reduced by placing the radar aside instead of in front of the measured slope and by applying the following equations (Addie, 1968):

$$\alpha_{app} = \tan^{-1}(\tan \alpha \times \sin \omega), \tag{6}$$

$$\omega = \omega_{LoS} - \omega_{slope}, \tag{7}$$

with  $\omega$  being the angle between the slope direction and the LoS direction, and  $\omega_{LoS}$  and  $\omega_{slope}$  being the orientation of

the LoS toward north and the slope strike, respectively. Table 2 lists the advantages and drawbacks of each radar position.

**2.3 Shadow, foreshortening, and layover**

The following three geometrical notions must be restated about radar geometry because they can trigger noise and/or loss of information (Jensen, 2006):

- *Foreshortening.* Any terrain with a slope  $\alpha$  inclined toward the radar (fore slope) results in a compression and a brightening of its surface in the radar image, also called foreshortening. Conversely, slopes inclined away from the radar (back slope) appear darker and elongated in the image (Fig. 8a). The foreshortening factor  $F_f$  can be defined as follows:
 
$$F_f = \sin(\alpha - \Phi). \tag{8}$$
- *Layover.* If the fore slope angle is greater than the look angle  $\Phi$ , then one can observe layover. The backscatter signal of the layover object will reach the radar receiver before the backscatter signal of the object located before. The information contained in the signal will be stored in the previous pixel in the range of the image, resulting in a layover distortion of the image which cannot be corrected. With a GB-InSAR, layover effects occur in the case of an overhanging wall (Fig. 8b).
- *Shadow.* An area hidden by a slope or by any other feature is not illuminated by the radar and will not be seen in the radar image, resulting in a loss of information.



**Table 2.** Advantages and drawbacks of each radar position presented in Fig. 7.

Point	Location	Advantages	Drawbacks	Resulting radar image
P1	<ul style="list-style-type: none"> <li>– Range direction perpendicular to cliff strike</li> <li>– Long-range distance</li> </ul>	Large illuminated area, $D_{\text{slope}}$ .	<ul style="list-style-type: none"> <li>Poor range resolution; compression of information in range.</li> <li>Important features may not be resolved.</li> </ul>	
P2	<ul style="list-style-type: none"> <li>– Range direction perpendicular to cliff strike</li> <li>– Short-range distance</li> </ul>	Good range resolution; important features can be distinguished.	<ul style="list-style-type: none"> <li>Small illuminated area, <math>D_{\text{slope}}</math>; potentially more shadowing than with P1.</li> </ul>	
P3	<ul style="list-style-type: none"> <li>– Range direction not perpendicular to cliff strike (decrease apparent slope)</li> <li>– Short-range distance</li> </ul>	Smaller apparent dip and greater range resolution compared to P2.	<ul style="list-style-type: none"> <li>Some important features can be in shadow;</li> <li>LoS may not be parallel to the displacement, and the recorded displacement value may be less than the real one, assuming a displacement along the steepest slope.</li> </ul>	

This can be, for instance, a deep valley or the ground behind a tall building (Fig. 8c).

- The areas in shadow and those subject to a strong foreshortening.

### 3 Methodology

#### 3.1 GB-InSAR constrains

In a review, Caduff et al. (2015) present a list of points to carefully consider when choosing the location for the GB-InSAR installation, including the visibility of the target area, the SoI, the foreshortening effects, the expected displacement (rate, direction, and mechanism), the atmospheric influences, and the technical constraints (hardware, setup, accessibility, etc.).

The MATLAB tool presented here is aimed at estimating some of those parameters and choosing the best location when several options are possible. The constraints estimated with the tool are the following:

- The range distance  $d_{\text{LoS}}$ ; the bandwidth (BW) must be adjusted based on this distance. In any case, the target should not be further than 4 or 5 km away, depending on the GB-InSAR device, to avoid the risk of a backscatter signal amplitude that is too weak.
- The resolution in range and in azimuth; once the potential location is found, it is worth estimating the resolution that will be obtained, as well as the extent of the surface illuminated by the radar.

#### 3.2 Input parameters

##### 3.2.1 The DEM

The MATLAB tool requires as first input a digital elevation model (DEM) in ASCII format that is cropped around the area of interest. The MATLAB code converts it into a 3D point cloud which is displayed in a window. For the use that will be made of the DEM, a resolution of 5 m is sufficient. For each pixel of the grid, the dip and dip direction is calculated with the function “gradient” (MATLAB, 2023). Additionally, the user provides the coordinates of the centre of the area of interest and of the location where they consider installing the radar.

##### 3.2.2 Radar parameters

The parameters that will be estimated are related to the radar characteristics described above ( $L$ ,  $BW$ , and  $\varepsilon$ ) and must be set up by the user before starting the computation because they influence the resulting resolution, as well as the extent of the illuminated area. Since the vertical beamwidth is limited in the case of the GB-InSAR, the vertical and horizontal beamwidths are, respectively, selected by the user and denoted  $\varepsilon_v$  and  $\varepsilon_h$ .

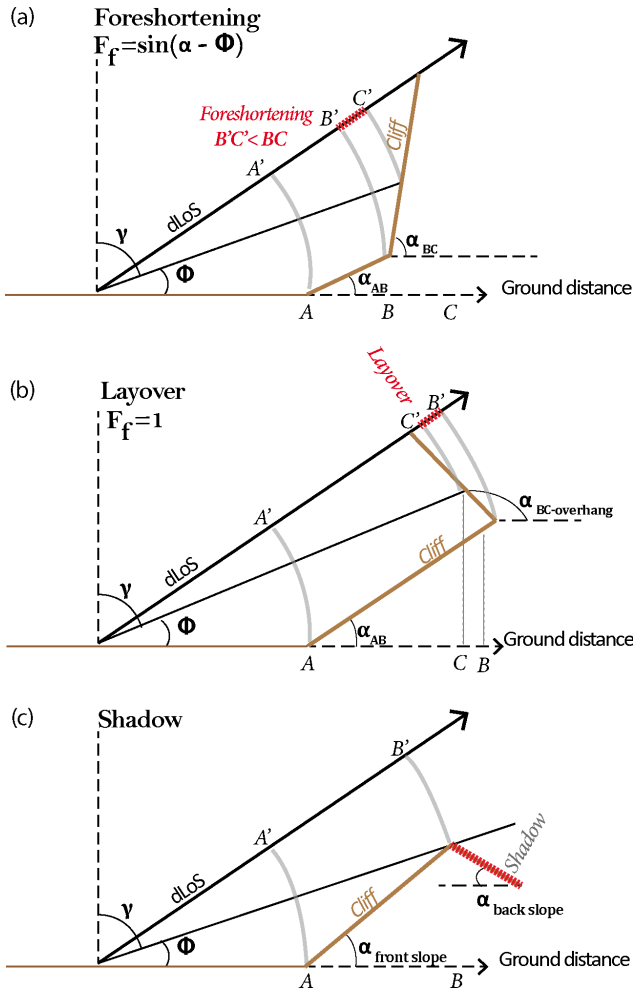


**Figure 8.** Illustration of geometrical artefacts in the case of GB-InSAR. (a) Foreshortening. (b) Layover. (c) Shadow effects.

### 3.3 Estimation of output radar results

#### 3.3.1 Fore slope and distance maps

First, when installing the radar, the distance between the radar and the target surface must be estimated to not be greater than 4 or 5 km. Once the location of the radar ( $x_{\text{radar}}$ ,  $y_{\text{radar}}$ , and  $z_{\text{radar}}$ ) is provided, a map is displayed that gives for each point of coordinates ( $x_{\text{target}}$ ,  $y_{\text{target}}$ , and  $z_{\text{target}}$ ) the distance to the radar, which is defined by

$$\text{distance} = \sqrt{\Delta x^2 + \Delta y^2 + \Delta z^2}, \quad (9)$$

with  $\Delta x = x_{\text{target}} - x_{\text{radar}}$ ,  $\Delta y = y_{\text{target}} - y_{\text{radar}}$ , and  $\Delta z = z_{\text{target}} - z_{\text{radar}}$ . Slopes facing the radar – or fore slope – can result in foreshortening effect, whereas slopes facing away – or back slope – will always be in the shadow. That information is displayed in a second map, where the fore slope points have a value of 1, and the other points have a value of  $-1$ . To produce this map, the apparent dip  $\alpha_{\text{app}}$  is computed for each

point with Eq. (6). The fore- and back slopes are deduced from  $\alpha_{\text{app}}$  as follows:

$$\text{If } \alpha_{\text{app}} > 0 \rightarrow \text{fore slope.} \quad (10)$$

$$\text{If } \alpha_{\text{app}} < 0 \rightarrow \text{back slope.} \quad (11)$$

#### 3.3.2 Radar footprint and illuminated area estimation

The radar footprint is an ellipse within which the user selects a smaller area to focus the radar acquisition. This illuminated surface is selected by choosing the minimum and maximum azimuth  $Az_{\text{min}}^{\circ}$  and  $Az_{\text{max}}^{\circ}$  and the minimum and maximum range  $R_{\text{min}}$  and  $R_{\text{max}}$  of the acquisition and should encompass the whole instable area to be monitored, as well as a supposedly stable area, in order to determine the necessary atmospheric corrections (Noferini et al., 2005; Pipia et al., 2008) and the post-processing unwrapping (Goldstein et al., 1988).

Before installing the radar and starting the acquisition, it is worth checking the maximum possible radar footprint, as well as the illuminated surface, according to the batch of azimuths and ranges selected by the user.

Once the radar and the target location are selected, the map is updated to display the footprint and the points illuminated by the radar during the acquisition according to the parameters  $R_{\text{min}}$ ,  $R_{\text{max}}$ ,  $Az_{\text{min}}^{\circ}$ , and  $Az_{\text{max}}^{\circ}$  selected by the user.

To do so, the coordinates of each point of the point cloud are converted from the global geographical coordinate system “global” in a local coordinate system “local”, whose frame origin is the centre of the region of interest selected by the user. The  $X$  axis is horizontal and perpendicular to the LoS direction, and the horizontal  $Y$  axis is perpendicular to  $X$ . The  $Z$  axis is a vertical unit vector. Thus, the unit vectors of the local frame are

$$\begin{pmatrix} X_{\text{unit}} \\ Y_{\text{unit}} \\ Z_{\text{unit}} \end{pmatrix}_{\text{local}} = \begin{pmatrix} \frac{\Delta y_{\text{global}}}{\sqrt{\Delta y_{\text{global}}^2 + \Delta x_{\text{global}}^2}} & \frac{\Delta x_{\text{global}}}{\sqrt{\Delta y_{\text{global}}^2 + \Delta x_{\text{global}}^2}} & 0 \\ \frac{\Delta x_{\text{global}}}{\sqrt{\Delta y_{\text{global}}^2 + \Delta x_{\text{global}}^2}} & \frac{\Delta y_{\text{global}}}{\sqrt{\Delta y_{\text{global}}^2 + \Delta x_{\text{global}}^2}} & 0 \\ 0 & 0 & 1 \end{pmatrix}. \quad (12)$$

Each point coordinate can be converted from the global geographical coordinate system to the new local coordinate system by applying a translation  $T$  defined by the vector

$$\text{LoS} \begin{pmatrix} \Delta x_{\text{global}} \\ \Delta y_{\text{global}} \\ \Delta z_{\text{global}} \end{pmatrix}, \text{ followed by a rotation of matrix } \Omega: \left\{ \begin{array}{l} T = \begin{pmatrix} \Delta x_{\text{global}} \\ \Delta y_{\text{global}} \\ \Delta z_{\text{global}} \end{pmatrix} \\ \Omega = \begin{pmatrix} a & -b & 0 \\ b & a & 0 \\ 0 & 0 & 1 \end{pmatrix} \end{array} \right. \quad (13)$$

The relation linking the coordinates of each point in the global geographical coordinate system and the new local coordinate system is

$$\begin{pmatrix} x \\ y \\ z \end{pmatrix}_{\text{local}} = \Omega \cdot \begin{pmatrix} x \\ y \\ z \end{pmatrix}_{\text{global}} + T \tag{14}$$

$$\begin{pmatrix} x \\ y \\ z \end{pmatrix}_{\text{local}} = \underbrace{\begin{pmatrix} a & -b & 0 \\ a & b & 0 \\ 0 & 0 & 1 \end{pmatrix}}_{\text{rotation matrix}} \cdot \begin{pmatrix} x \\ y \\ z \end{pmatrix}_{\text{global}} + \underbrace{\begin{pmatrix} \Delta x_{\text{global}} \\ \Delta y_{\text{global}} \\ \Delta z_{\text{global}} \end{pmatrix}}_{\text{translation matrix}} \tag{15}$$

The pair of values  $(a, b)$  is found by solving the system with the coordinates of the target point  $\begin{pmatrix} 0 \\ 0 \\ 0 \end{pmatrix}_{\text{local}}$  in the local coordinate system:

$$\begin{pmatrix} 0 \\ 0 \\ 0 \end{pmatrix}_{\text{local}} = \begin{pmatrix} a & -b & 0 \\ b & a & 0 \\ 0 & 0 & 1 \end{pmatrix} \cdot \begin{pmatrix} x_{\text{target}} \\ y_{\text{target}} \\ z_{\text{target}} \end{pmatrix}_{\text{global}} + \begin{pmatrix} \Delta x_{\text{global}} \\ \Delta y_{\text{global}} \\ \Delta z_{\text{global}} \end{pmatrix} \tag{16}$$

All points of the point cloud are converted into the new local coordinate system with Eq. (13). It is then possible to filter points that belong to the radar footprint, knowing  $\varepsilon_v$  and  $\varepsilon_h$  (Fig. 9a). A point  $P(x_{\text{local}}, y_{\text{local}}, z_{\text{local}})$  is within the footprint if

$$|z_{\text{local}}| < \sqrt{H_\varepsilon^2 - \left(\frac{x_{\text{local}}}{L_\varepsilon}\right)^2} \tag{17}$$

with

$$L_\varepsilon = \text{dLoS}(O) \cdot \tan \varepsilon_h \tag{18}$$

$$H_\varepsilon = \text{dLoS}(O) \cdot \tan \varepsilon_v. \tag{19}$$

Points belonging to the illuminated area are extracted in a second step. A point  $P(x_{\text{local}}, y_{\text{local}}, z_{\text{local}})$  is within the illuminated area if (Fig. 9b)

$$\begin{cases} P \in \text{footprint} \\ \text{dLoS}(P) \in [R_{\text{min}}; R_{\text{max}}] \\ z_{\text{local}} \in [W_{\text{min}}(P); W_{\text{max}}(P)] \end{cases}, \tag{20}$$

with

$$\begin{cases} W_{\text{illu}_{\text{min}}}(P) = \text{dLoS}(P) \cdot \tan Az^{\circ}_{\text{min}} \\ W_{\text{illu}_{\text{max}}}(P) = \text{dLoS}(P) \cdot \tan Az^{\circ}_{\text{max}} \end{cases}. \tag{21}$$

Once the points illuminated by the radar are known, a mean square method (Wolberg, 2006) is used to determine the mean plan intersecting the illuminated points defined by its normal vector  $N$ . This vector is then converted into the mean slope dip  $\alpha_{\text{MEAN}}$  and the mean slope dip direction  $\omega_{\text{MEAN}}$ .

### 3.3.3 Resolution, foreshortening, and layover maps

Equations (1) and (4) are applied on each point of the point cloud to estimate the range and azimuthal resolutions, and the result is displayed in two distinct maps.

With the mean plan dip direction  $\omega_{\text{MEAN}}$  and dip  $\alpha_{\text{MEAN}}$  being known, the latter is converted in apparent dip from the radar position  $\alpha_{\text{MEAN\_app}}$ , and the foreshortening for this mean plan  $F_{F\text{-MEAN}}$  is calculated by applying Eq. (8), giving a value comprised between  $[0; 1]$ , with 0 for no foreshortening and 1 for the beginning of layover. In addition, the foreshortening degree is calculated for each point of the point cloud.

It is then possible to estimate for each point if it will be affected by a stronger or a weaker foreshortening than the mean slope plan by subtracting the mean plan foreshortening  $F_{F\text{-MEAN}}$  from the foreshortening calculated at each point. Such a map is also one of the outputs of the tool. A negative or positive value implies, respectively, a weaker or stronger foreshortening at that point than the mean one.

### 3.4 Tool interface

The application coded in MATLAB is presented in a graphical user interface (Fig. 10). The users first select the DEM to import and convert into a 3D point cloud. They then give the coordinates of the location where they consider installing the radar, as well as the coordinates corresponding to the center (or middle) of the region of interest. It can be found directly on the point cloud or from a GPS measurement performed on the field. The radar parameters, listed in Table 3, must also be given before starting the computation. To filter pixels within the area illuminated during the processing, the user also gives the minimum and maximum ranges and azimuths.

At the end of the processing, the different maps are displayed in 3D and can be saved as a text file to be reused later.

## 4 Description of the tested case studies

To validate the results obtained with this tool, the latter has been tested with a Lisalab GB-InSAR (Table 3) on (1) a simple synthetic cliff created in CloudCompare, facing north and with a progressive slope and a back slope (Fig. 11), and (2) two real cliffs where GB-InSAR monitoring campaigns were conducted (Table 4; Figs. 12 and 13).

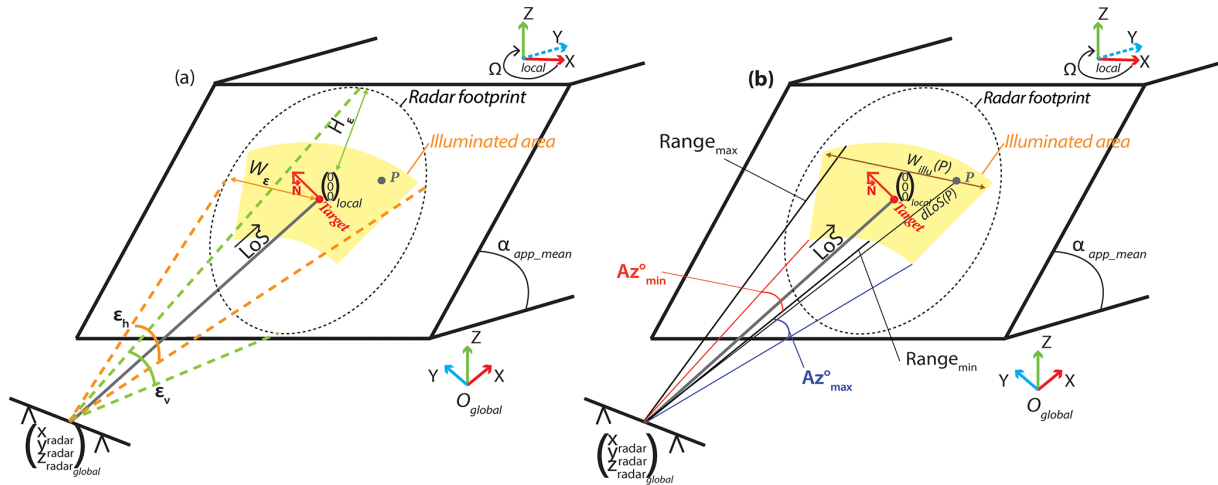
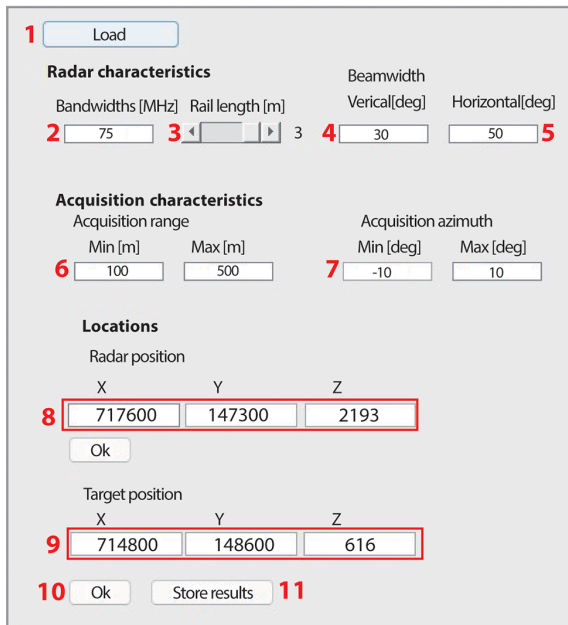


**Figure 9.** Illustration of the change in the coordinate frame from a global one  $(X, Y, Z)_{global}$  to a local one  $(X, Y, Z)_{local}$ , centred on the target coordinates and aiming at highlighting the points of the point cloud within the radar footprint and the illuminated area. The  $X_{local}$  axis is horizontal and perpendicular to  $LoS$ , and the  $Y_{local}$  axis is horizontal and perpendicular to  $X_{local}$ . (a) Point  $P$  is within the radar footprint because its coordinates answer the conditions defined in Eq. (16). (b) Point  $P$  is illuminated because its coordinates answer the conditions defined in Eq. (19).



**1- Load DEM ascii format**

```

    1 ncols 98
    2 nrows 87
    3 xllcorner 714824
    4 yllcorner 146286
    5 cellsize 50
    6 NODATA_value -999
    7 1122 1103 1081 1066 1047 1027 1008 976 952 928 902 865
    8 1116 1102 1082 1064 1049 1032 988 971 960 923 897 873
    9 1110 1083 1065 1045 1029 1014 993 966 943 904 878 859
    10 1090 1067 1048 1029 1011 993 971 952 928 925 885 858
    11 1078 1074 1049 1030 1011 992 971 951 925 880 865 845
    12 1058 1038 1033 1013 996 973 955 928 900 880 865 853
    13 1051 1042 1014 993 994 955 932 908 889 874 857 847
    14 1045 1021 1001 981 957 954 936 913 895 885 869 850
    15 1030 1001 983 977 965 945 920 903 894 880 859 841
    
```

- 2 - Radar bandwidth BW**
- 3 - Rail length used for focusing the signal L**
- 4 - Radar vertical beamwidth  $\epsilon_v$  (limited to 30°)**
- 5 - Radar horizontal beamwidth  $\epsilon_h$  (limited to 50°)**
- 6 - Radar acquisition min/max range**
- 7 - Radar acquisition min/max azimuth**
- 8 - Coordinate radar location**
- 9 - Coordinate target location**
- 10 - Validate coordinates and start processing**
- 11 - Save output as text file**

**Figure 10.** Interface of the MATLAB tool and the format of the DEM grid to import in a text file format.

**4.1 Real case 1: Cima del Simano instability monitoring**

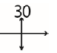
Cima del Simano is a deep-seated landslide located in the Ticino canton in Switzerland (Fig. 12a). Satellite interferometry measurements highlight the presence of slow sub-vertical gravitational movements on top of the mountain which motivated the launch of a GB-InSAR monitoring campaign in 2021 (Wolff et al., 2023). A Lisalab GB-InSAR with a 3 m rail was installed in the valley near a building belonging to

the Acquarossa commune in order to have access to an electrical power supply (Fig. 12c). The acquisition is challenging because the radar is located at its range limit, and the top of the cliff, at an altitude of 2500 m, witnesses strong atmospheric effects (Fig. 12b).

**4.2 Real case 2: La Cornalle cliff monitoring**

La Cornalle cliff, located in the Lavaux vineyard (east Lausanne, Switzerland; Fig. 13a), has been monitored with

**Table 3.** Characteristics of the LiSA GB-InSAR used in this study.

Radar system	Rail length $L$ [m]	Antenna type	Maximal horizontal/vertical beamwidth $\varepsilon_h/\varepsilon_v$ [°]	Radar band	Central pulse frequency $f$ [GHz]	Bandwidth BW [MHz]	Measurable phenomena max speed [mm h <sup>-1</sup> ]
Lisalab	3	Horn antenna	50 	Ku band	17.2	[50–175]	176

**Table 4.** The three study cases with their DEM characteristics and the radar parameters chosen.

Case study	Geographical coordinate system	Radar location [m]	Target location [m]	Distance estimation [m]	BW [Mhz]	Min/max ranges [m]	Min/max azimuths [°]
1 – synthetic dataset	–	$x - 0$ $y - 100$ $z - 1$	$x - 0$ $y - -88$ $z - 20$	200	175	180/205	-12/12
2 – Cima del Simano	CH1903 LV03	$x - 714\,800$ $y - 148\,600$ $z - 616$	$x - 717\,600$ $y - 147\,300$ $z - 2193$	3500	75	3100/4200	-9/9
3 – La Cornalle	CH1903 LV03	$x - 547\,000$ $y - 149\,000$ $z - 230$	$x - 548\,000$ $y - 150\,000$ $z - 685$	200	175	140/250	-4/4

yearly lidar acquisitions since 2013 (Carrea et al., 2014, 2015). This steep cliff is affected by erosion processes, and frequent rockfall events occur every year (Fig. 13b). This site is monitored to estimate the role of the rock surface temperature and of the atmospheric erosion (Fei et al., 2023). For this purpose, a GB-InSAR has been installed in August 2022 at the bottom of the cliff. The Lisalab rail has been set up on a flat wall near a factory in the vineyard to have access to electricity and also very near the cliff to get the best possible resolution (Fig. 13c).

## 5 Results

The obtained results are summarized in Table 5 for the three studied cases, and some output maps are displayed in Fig. 14 in the case of the synthetic dataset, in Fig. 15 in the case of Cima del Simano, and in Fig. 16 for La Cornalle cliff. The extra output maps are available in Figs. A1–A3.

### 5.1 Synthetic dataset (Figs. 14 and A1)

With a LoS distance of 200 m, the range and azimuthal resolutions are, respectively, 0.95 and 0.57 m at the target location. The calculated apparent mean dip is 48° because the illuminated area encompasses a major part of the slope with a dip of 40° and a little part of the slope with a dip of 70°. The mean foreshortening of the SoI is 0.67 (Fig. 14e), but the

points located on the slope with a dip of 40° are less affected by foreshortening than those located on the slope with a dip of 70° (Fig. 14f).

### 5.2 Cima del Simano (Figs. 15 and A2)

The LoS distance is almost at the limit of what is acceptable to have for a backscattered signal (3351 m at the target location and 3900 m near the crest). Such a distance decreases the azimuthal resolution considerably, which varies between 8 and 13 m along the range of the illuminated slope (Fig. 15c) for a range resolution of 2.0 m (Fig. 15d). The SoI is affected by a constant and low foreshortening of 0.38 (Fig. 15e and f).

### 5.3 La Cornalle (Figs. 16 and A3)

The LoS distance is 267 m, resulting in a good resolution in the azimuth varying between 0.3 and 0.7 m along the SoI (Fig. 16c) and in the range between 0.8 and 1 m (Fig. 16d). The slope is very steep, and the apparent slope dip is 73°. Consequently, the radar image is affected by a strong foreshortening of 0.81 (Fig. 16e). In the centre of the slope illuminated by the radar (Fig. 16a), one can see a little back slope terrace, which is consequently affected by shadowing (Fig. 16b). The slope below this terrace is less steep than the illuminated area mean plan, oriented 61/267°, while the one located above is steeper. The lower part is less affected by foreshortening than the upper part (Fig. 16f).

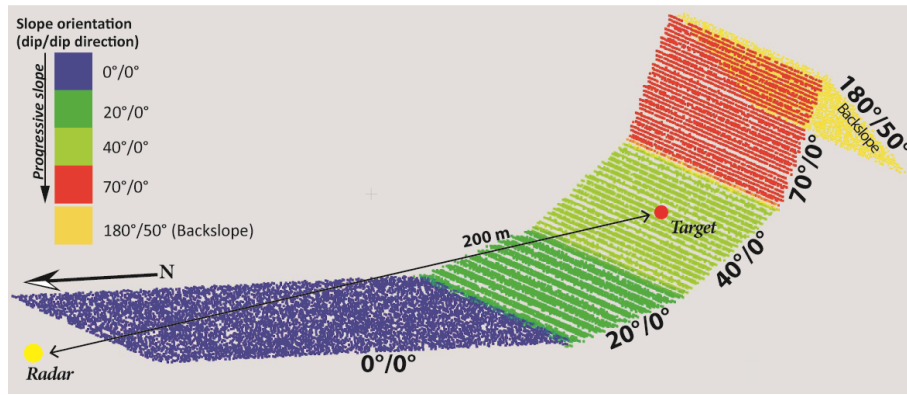


Figure 11. Synthetic dataset of a cliff facing north with a progressive slope dip and a back slope.

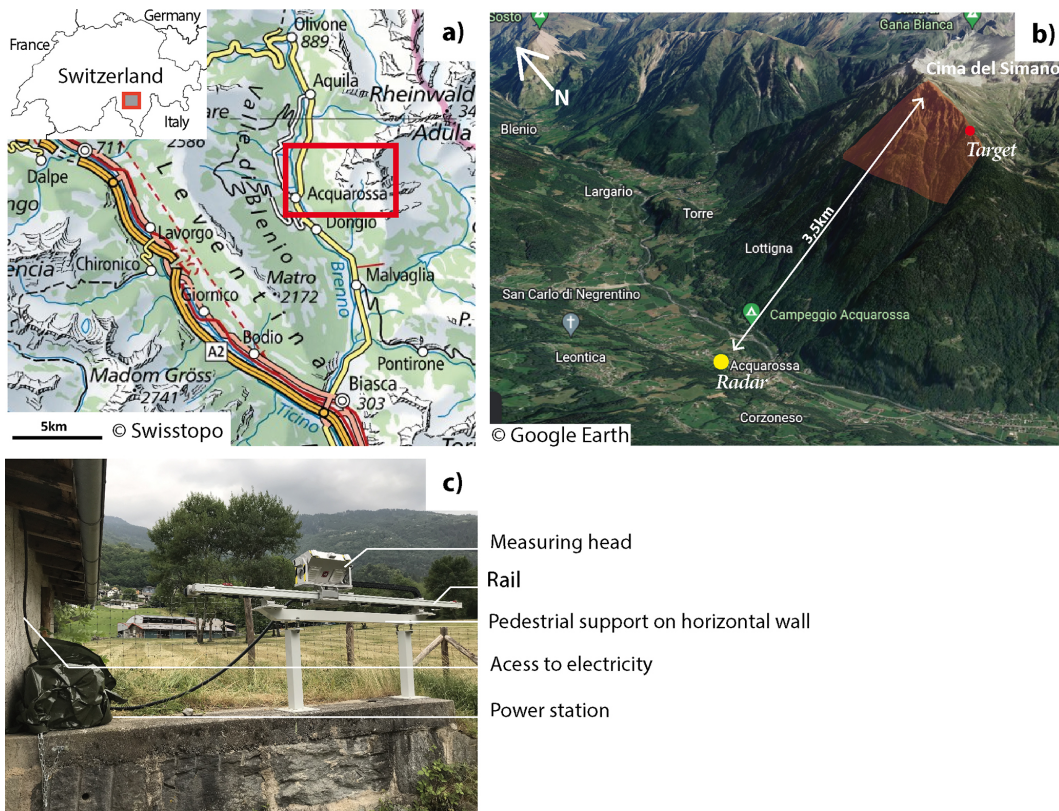


Figure 12. First real studied site at Cima del Simano. (a) Location. (b) Radar and target location shown in the Google Earth © 2022 image. (c) Lisalab GB-InSAR installation.

6 Discussion

6.1 Comparison for three different radar locations

Figure 7 presented the impact of the radar location on the resulting image. To verify those concepts, three radar locations, P1, P2 and P3, have been selected at the study site of Cima del Simano to monitor the same region of interest. Their output characteristics are summarized and compared in Table 6. Locations P1 and P2 are located in front of the cliff

and along the direction parallel to the slope dip; P1 is further away from the target area than P2. P3 is located almost at the same distance of the cliff as P2 (P3 is 113 m further away from the target than P2) but faces the target area from the side.

The results are coherent with what is expected from Table 2. An acquisition from P2 gives a better range resolution (2.01 m) compared to P1 (2.14 m). Those two points are located in front of the cliff, and their apparent slope dip cor-

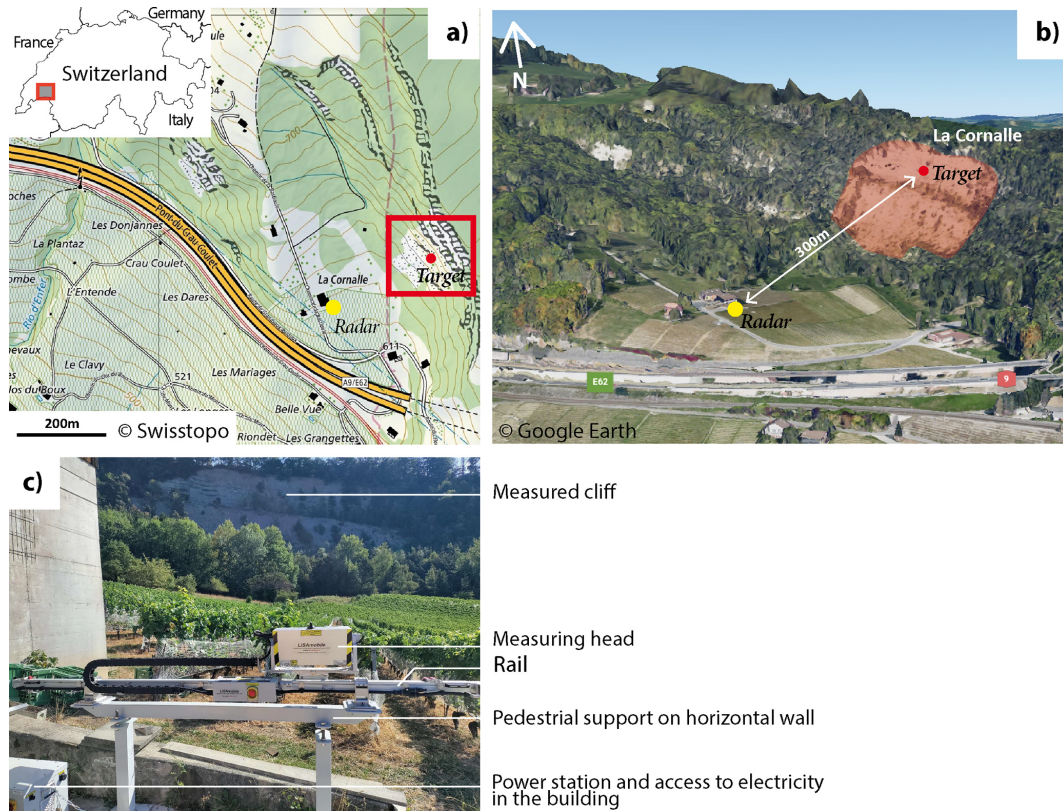


**Figure 13.** Second real studied site at La Cornalle cliff. (a) Location. (b) Radar and target location shown in the Google Earth © 2022 image. (c) Lisalab GB-InSAR installation.

**Table 5.** Results obtained with the MATLAB tool for the three study sites.

Case study	Location	Range resolution [m]	Azimuthal resolution [m]	dLoS [m]	Mean dip	Mean dip direction	Mean foreshortening	Output maps
0	Synthetic dataset	0.95	0.57	200	48°	0°	0.67	Fig. 14
1	Cima del Simano	2.0	10.4	3351	51°	344°	0.38	Fig. 15
2	La Cornalle	0.92	0.64	267	61°	201°	0.81	Fig. 16

responds to the real one (64°), while the apparent slope dip for P3 is lower (60°), slightly reducing the range resolution (2.00 m). One could conclude that the best location for the acquisition is P3. Nonetheless, this position triggers more areas in the shadow (back slope), leading to a loss of information. Furthermore, the gravitational movements are often expected to follow the slope dip direction (Dehls et al., 2010; Pedrazzini et al., 2010). Looking at the target area from the side, as with P3, the LoS direction is not parallel to the slope, and the registered displacement may be less than the real one (Colesanti and Wasowski, 2006; Dai et al., 2022).

The illuminated area is wider in the case of P1 than P2 or P3. If the unstable area to monitor is very large, P1 can be advantageous. Since the LoS distance remains smaller

than 4 km (3.9 km), the backscattered signal is still registered from P1.

Thus, the best installation location highly depends on the purpose of the acquisition and the area of interest.

- If the main goal is to monitor a large area in order to detect unstable zones and estimate an average displacement rate, such as in Carlà et al. (2019), a position far from the monitored cliff (similar to P1) should be considered. The tool can help check that the LoS distance remains shorter than 4 or 5 km and estimate the extent of the illuminated area. But one must be aware that the resulting range and azimuthal resolutions of the radar will be worse than at location P1.

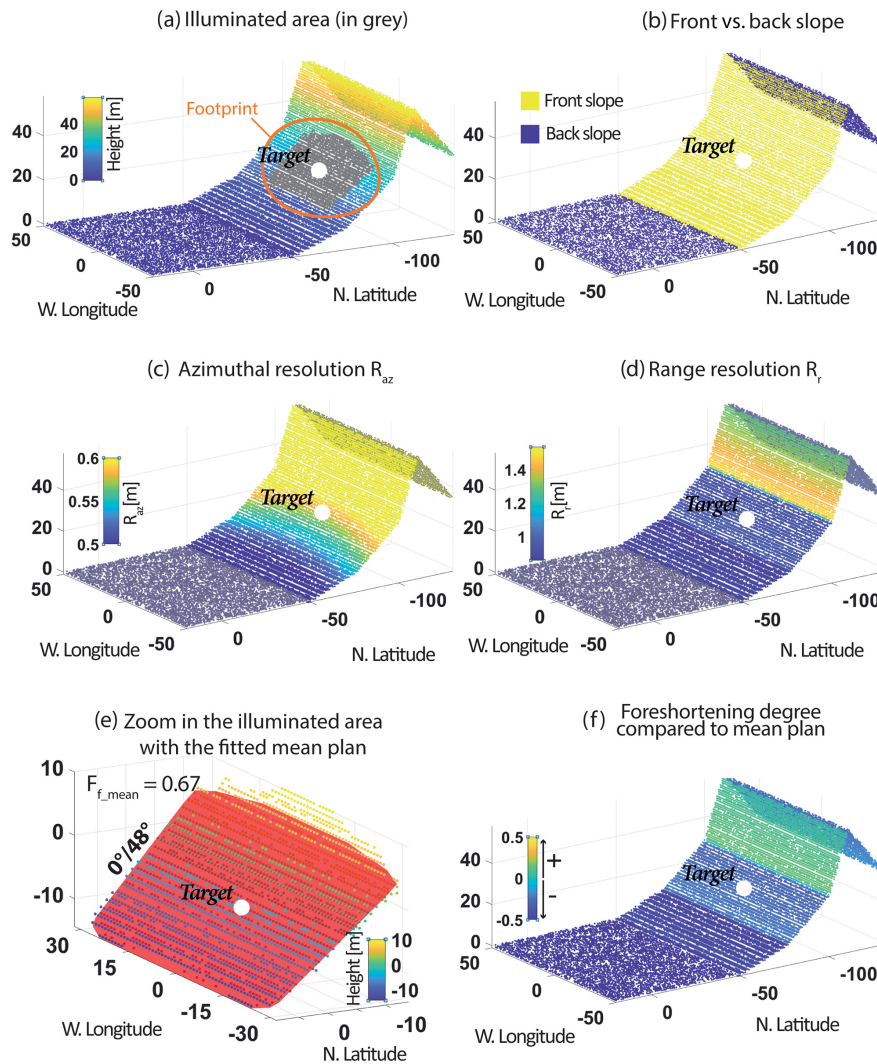


**Figure 14.** Output maps for the synthetic dataset. **(a)** Illuminated area and footprint for the chosen parameters. **(b)** Front vs. back slope. The back slope corresponds to areas in the shadow. **(c)** The azimuthal resolution increases with the distance to the radar. **(d)** The range resolution increases with the slope dip, but at the same slope degree, it decreases from the near- to far-range. **(e)** Zoomed-in view of the illuminated area for which the mean plan is estimated. The mean dip of the area is  $48^\circ$  with a mean foreshortening of 0.67. **(f)** Foreshortening degree compared to the mean plan  $F_{f\_MEAN}$ . Smoother slopes are less affected by the foreshortening than the mean plan. The steeper ones are more affected. The other output maps are presented in Fig. A1.

- If the main goal is to get the best resolution at the expense of the illuminated area size, one should try locating the radar closer to the monitored cliff (similar to P2 and P3). It is the case, for example, when one tries to define the kinematic behaviour (Frattini et al., 2018) or assess the susceptibility of massive rock instabilities to fail (Jaboyedoff et al., 2012). The tool helps check which location (close to, in front of, or aside the cliff) gives the best resolution while avoiding having the Sol in the shadow.

## 6.2 Tool limitations

Since the input of the program is a DEM converted into a 3D grid, the overhanging slopes, which are those subject to layover, cannot be detected. To overcome this limitation, a suggestion could be to use a point cloud acquired from the ground with a lidar (Abellán et al., 2014) or by photogrammetry (Eltner and Sofia, 2020). But this comes with other problems, such as potential occlusions (Sturzenegger et al., 2007) and noises due to the presence of vegetation which can bias the calculated dip and dip direction of the slope.



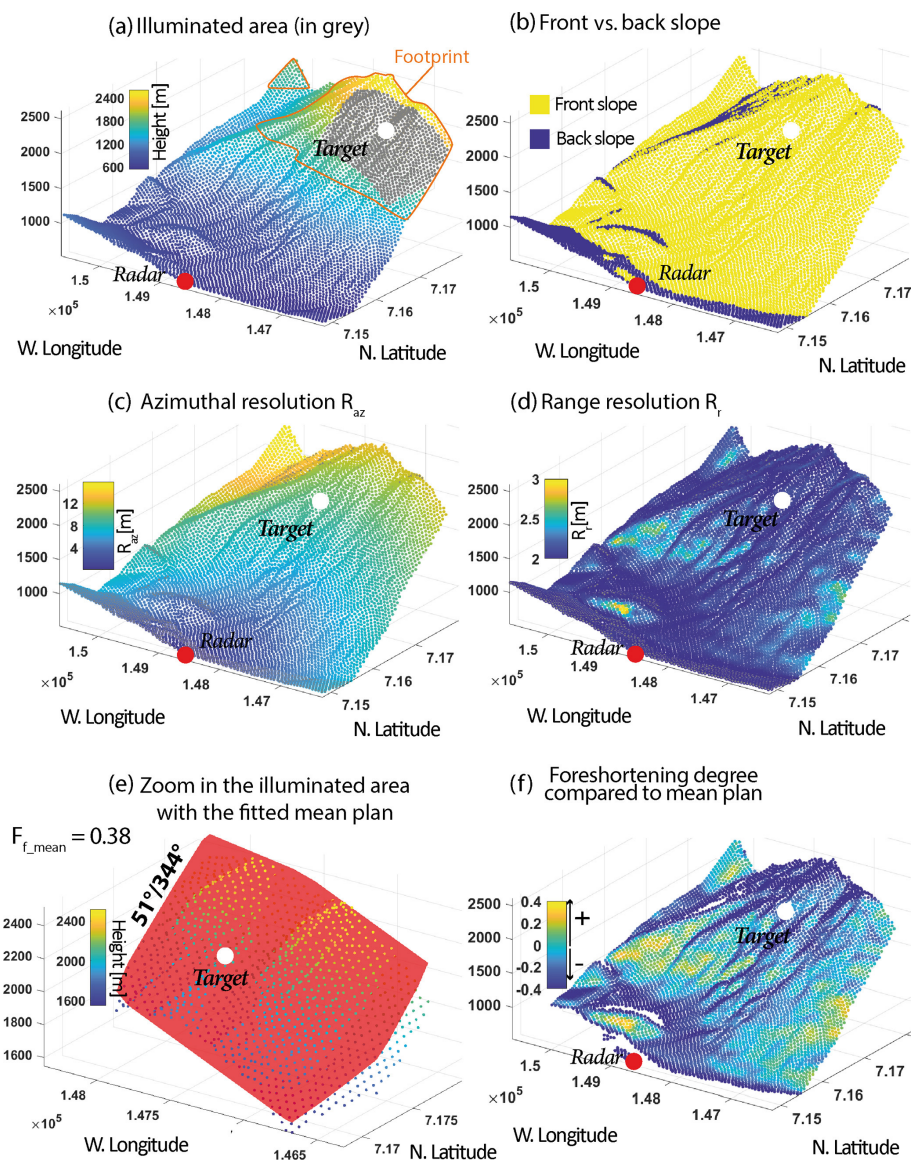


**Figure 15.** Output maps for the first dataset of Cima del Simano. **(a)** Illuminated area and footprint for the chosen parameters. **(b)** Front vs. back slope. The back slope corresponds to areas in the shadow. **(c, d)** Azimuthal and range resolutions. Since the chosen bandwidth is 75 MHz to be sure to record the backscattered signal, the resolutions are poor. Only a monitoring of the major volume instabilities is relevant here. **(e)** Zoomed-in view of the illuminated area for which a mean plan fitting is estimated. The mean dip of the area is  $51^\circ$  with a mean foreshortening of 0.38. **(f)** Foreshortening degree compared to the mean plan. The lower part is more affected by foreshortening at the top of the mountain which is the area of interest. The other output maps are presented in Fig. A2.

## 7 Conclusion and further development

This paper described the main features of a linear GB-InSAR acquisition, emphasizing and comparing the significant differences from satellite radar acquisitions. While these distinctions are rarely addressed in the literature, they are crucial considerations for anyone initiating a GB-InSAR monitoring campaign.

The paper introduces in a second step a novel MATLAB tool designed for the estimation of the characteristics of lin-

ear GB-InSAR acquisitions. This tool generates a set of valuable maps, including the radar-to-target distance, range and azimuthal resolution, foreshortening degree, and shadowing maps in a single operation. The main purpose is to streamline the search for the optimal radar installation site which guarantees the most effective monitoring results when multiple options are considered.

Since the determination of the ideal location varies depending on the objectives of the acquisition campaign, pro-

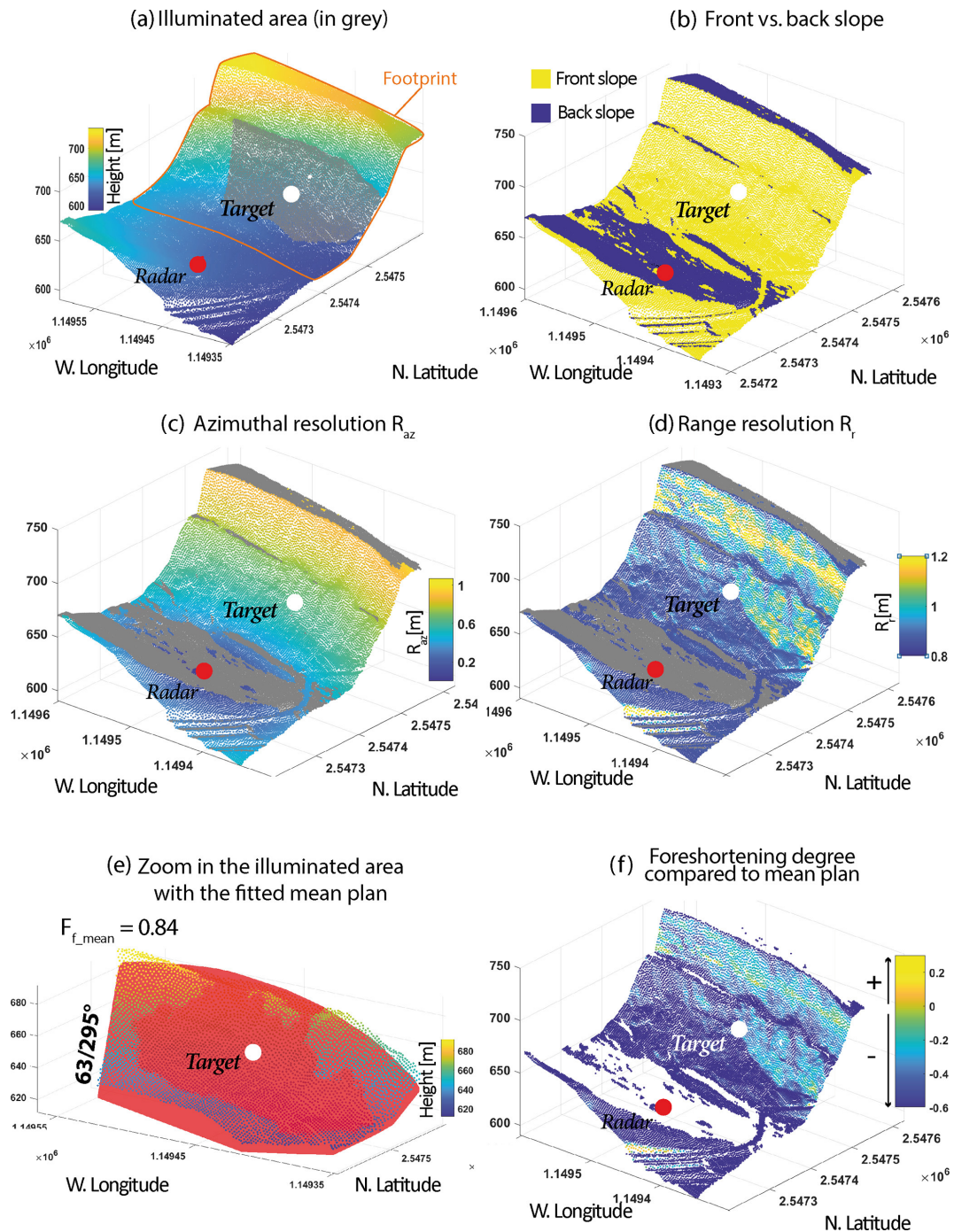


**Figure 16.** Output maps for the second dataset at La Cornalle cliff. (a) Illuminated area and footprint for the chosen parameters. (b) Front vs. back slope. The back slope corresponds to areas in the shadow. (c, d) Azimuthal and range resolutions. Since the radar is only at a distance of 260 m, the selected bandwidth is 175 MHz to have a good range resolution. (e) Zoomed-in view of the illuminated area for which a mean plan fitting is estimated. The mean dip of the area is  $61^\circ$  with a mean foreshortening of 0.81. (f) Foreshortening degree compared to the mean plan. The other output maps are presented in Fig. A3.

**Table 6.** Comparison of three different radar locations and the impact on their corresponding radar image. Advantages and drawbacks for each position are highlighted.

Corresponding position in Fig. 7 test case	P1 in front of the cliff and far from the cliff	P2 in front of the cliff and close to the cliff	P3 aside the cliff
Coordinate system	CH1903-LV03		
Target location	[717 600; 147 300; 2193]		
Radar location	[714 108; 148 128; 750]	[715 400; 148 700; 635]	[715 201; 147 193; 556]
Back slope			
Illuminated area			
dLoS	3927	3282	3150
App. dip	64°	64°	60°
Azimuthal resolution	11.64	9.89	8.72
Range resolution	2.14	2.01	2.00
Advantages	– Wider extent of the illuminated surface	– Better resolutions than P1	– Better resolutions than P1 and P2
Drawbacks	– Compression of information in range – dLoS limit for recording backscattered signal	– Smaller illuminated surface than P1 – More shadow than P1	– More shadow than P1 and P2 – Measured displacement along the LoS may be lower than the real one

viding comprehensive information critical for selection simplifies the sensitive choice for the most suitable site.

If the purpose is to monitor a large area and to delimitate the unstable zone, then the radar should be installed far from the cliff, using the MATLAB tool to check that the LoS distance remains shorter than 4 or 5 km, depending on the GB-InSAR device. Contrariwise, if the purpose is to characterize the displacement gradient, one will try to optimize the resolution while keeping the LoS as parallel as possible to the displacement vector. In that case, the tool helps verify and avoid the foreshortening and shadowing areas.

Nevertheless, the radar acquisition characteristics are often not the only thing to consider when choosing the best location. Most of the time, the access to electricity and an easy installation on a flat surface, as well as the expected in-

stability movement direction, reduce the choices (Caduff et al., 2015).

The tool could be improved and extended to the other GB-InSARs of type ArcSAR or rotary RAR (Pieraccini and Miccinesi, 2019) and for the estimation of satellite InSAR image characteristics in order to select the best ascending or descending orbit acquisition before starting the downloading and treatment of the images which can also be long and laborious work (Berardino et al., 2002; Mancini et al., 2021).

## Appendix A

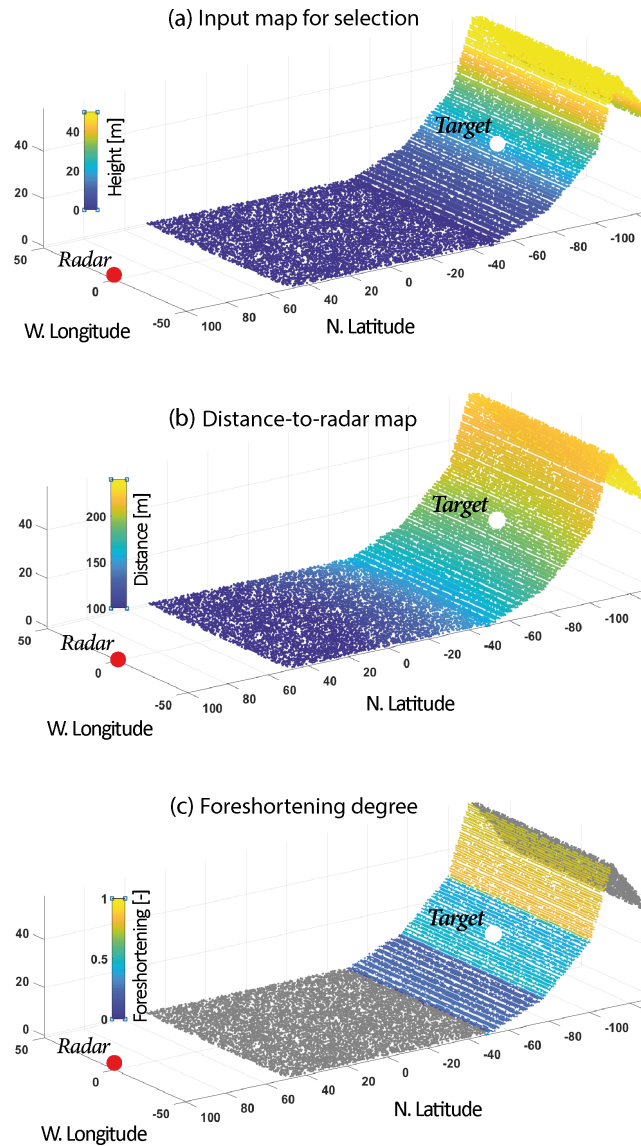


**Figure A1.** Additional output maps for the synthetic dataset. **(a)** The input map with the altitude that is aimed at choosing the radar and target location. **(b)** The distance-to-radar map. The distance between the radar and the target should not be greater than 4 km. **(c)** The foreshortening map, after Eq. (8).

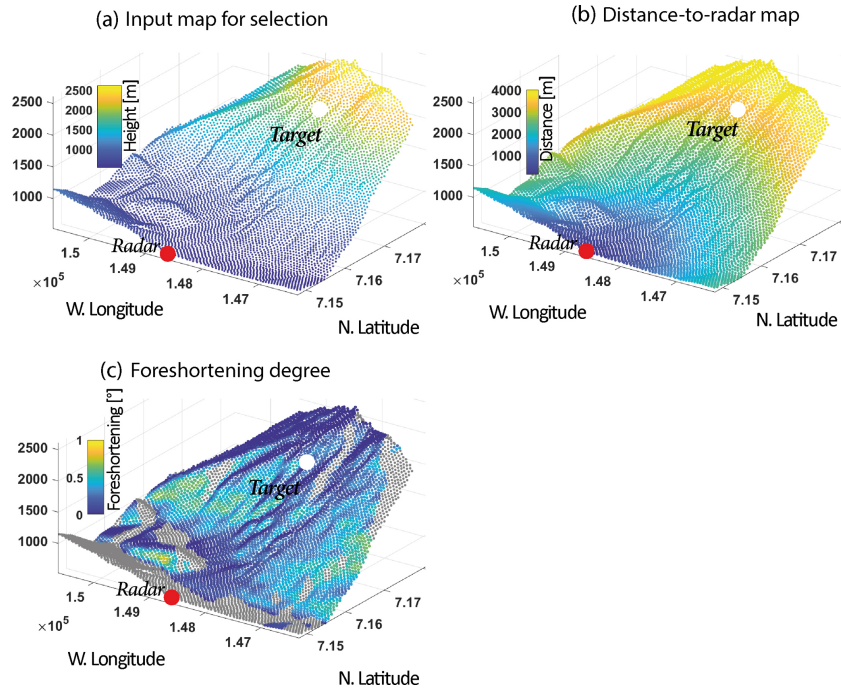


**Figure A2.** Additional output maps for the first real dataset; Cima del Simano. (a) The input map with the altitude is aimed at choosing the radar and target location. (b) The distance-to-radar map. The distance between the radar and the target should not be greater than 4 km. (c) The foreshortening map, after Eq. (8).

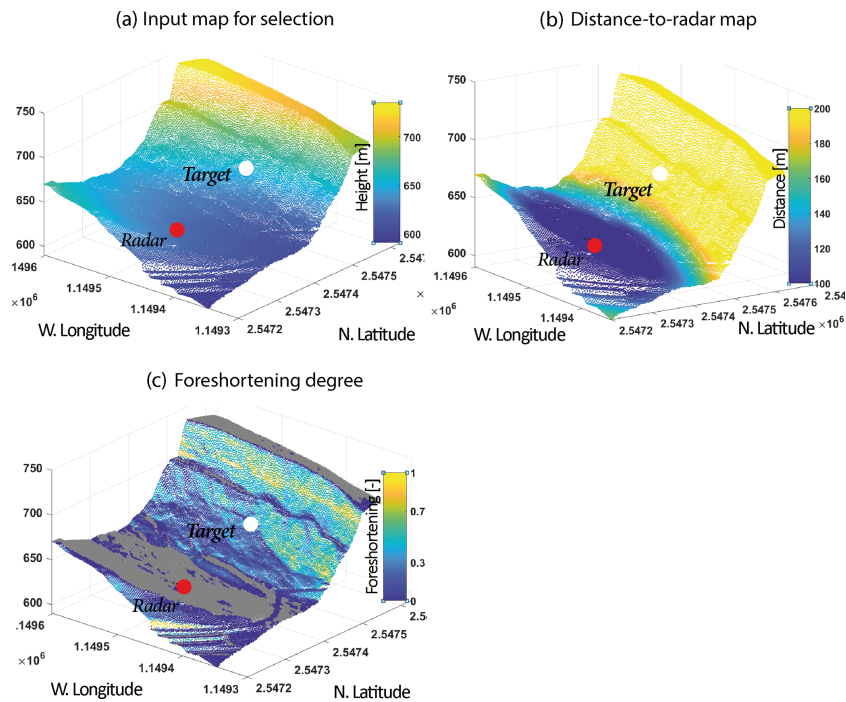


**Figure A3.** Additional output maps for the second real dataset; La Cornalle. (a) The input map with the altitude is aimed at choosing the radar and target location. (b) The distance-to-radar map. The distance between the radar and the target should not be greater than 4 km. (c) The foreshortening map, after Eq. (8).

*Code and data availability.* All raw data can be provided by the corresponding authors upon request. The code and the input point clouds are available on GitHub (<https://doi.org/10.5281/zenodo.12820384>, Wolff, 2024).

*Author contributions.* MHD had the tool idea. CW wrote and tested the code. CW created the synthetic dataset and performed the acquisition of the real datasets. CR provided the documentation for comparing satellite and GB techniques. CW wrote and edited the draft. MHD, CR, and MJ reviewed the paper.

*Competing interests.* The contact author has declared that none of the authors has any competing interests.

*Disclaimer.* Publisher's note: Copernicus Publications remains neutral with regard to jurisdictional claims made in the text, published maps, institutional affiliations, or any other geographical representation in this paper. While Copernicus Publications makes every effort to include appropriate place names, the final responsibility lies with the authors.

*Review statement.* This paper was edited by Anette Eltner and reviewed by two anonymous referees.

## References

- Abellán, A., Oppikofer, T., Jaboyedoff, M., Rosser, N. J., Lim, M., and Lato, M. J.: Terrestrial laser scanning of rock slope instabilities: State-Of-Science (Terrestrial Lidar Vs. Rock Slope Instabilities), *Earth Surf. Proc. Land.*, 39, 80–97, <https://doi.org/10.1002/esp.3493>, 2014.
- Addie, G.: A new true thickness formula based on the apparent dip, *Econ. Geol.*, 63, 188–189, <https://doi.org/10.2113/gsecongeo.63.2.188>, 1968.
- Anon: ETSI EN 300 440 v2.1.1, [https://www.etsi.org/deliver/etsi\\_en/300400\\_300499/300440/02.01.01\\_60/en\\_300440v020101p.pdf](https://www.etsi.org/deliver/etsi_en/300400_300499/300440/02.01.01_60/en_300440v020101p.pdf) (last access: 25 April 2024), 2017.
- Antonello, G., Casagli, N., Farina, P., Fortuny, J., Leva, D., Nico, G., Sieber, A. J., and Tarchi, D.: A ground-based interferometer for the safety monitoring of landslides and structural deformations, in: *IGARSS 2003, 2003 IEEE International Geoscience and Remote Sensing Symposium*, 21–25 July 2003, Toulouse, France, 218–220, <https://doi.org/10.1109/IGARSS.2003.1293729>, 2003.
- Berardino, P., Fornaro, G., Lanari, R., and Sansosti, E.: A new algorithm for surface deformation monitoring based on small baseline differential SAR interferograms, *IEEE T. Geosci. Remote.*, 40, 2375–2383, <https://doi.org/10.1109/TGRS.2002.803792>, 2002.
- Cabral-Cano, E., Dixon, T. H., Miralles-Wilhelm, F., Diaz-Molina, O., Sanchez-Zamora, O., and Carande, R. E.: Space geodetic imaging of rapid ground subsidence in Mexico City, *Geol. Soc. Am. Bull.*, 120, 1556–1566, <https://doi.org/10.1130/B26001.1>, 2008.
- Caduff, R., Schlunegger, F., Kos, A., and Wiesmann, A.: A review of terrestrial radar interferometry for measuring surface change in the geosciences: Terrestrial Radar Interferometry In The Geosciences, *Earth Surf. Proc. Land.*, 40, 208–228, <https://doi.org/10.1002/esp.3656>, 2015.
- Carlà, T., Tofani, V., Lombardi, L., Raspini, F., Bianchini, S., Bertolo, D., Thuegaz, P., and Casagli, N.: Combination of GNSS, satellite InSAR, and GBInSAR remote sensing monitoring to improve the understanding of a large landslide in high alpine environment, *Geomorphology*, 335, 62–75, <https://doi.org/10.1016/j.geomorph.2019.03.014>, 2019.
- Carrea, D., Abellán, A., Guerin, A., Jaboyedoff, M., and Voumard, J.: Erosion processes in molassic cliffs: the role of the rock surface temperature and atmospheric conditions, in: *EGU General Assembly 2014*, Geophysical Research Abstracts Vol. 16, EGU2014-9188-1, <https://meetingorganizer.copernicus.org/EGU2014/EGU2014-9188-1.pdf> (last access: 25 July 2024), 2014.
- Carrea, D., Abellan, A., Derron, M.-H., and Jaboyedoff, M.: Automatic Rockfalls Volume Estimation Based on Terrestrial Laser Scanning Data, in: *Engineering Geology for Society and Territory – Volume 2*, edited by: Lollino, G., Giordan, D., Crosta, G. B., Corominas, J., Azzam, R., Wasowski, J., and Sciarra, N., Springer International Publishing, Cham, 425–428, [https://doi.org/10.1007/978-3-319-09057-3\\_68](https://doi.org/10.1007/978-3-319-09057-3_68), 2015.
- Casagli, N., Farina, P., Leva, D., Nico, G., and Tarchi, D.: Ground-based SAR interferometry as a tool for landslide monitoring during emergencies, in: *IGARSS 2003, 2003 IEEE International Geoscience and Remote Sensing Symposium*, 21–25 July 2003, Toulouse, France, 2924–2926, <https://doi.org/10.1109/IGARSS.2003.1294633>, 2003.
- Catani, F., Canuti, P., and Casagli, N.: The Use of Radar Interferometry in Landslide Monitoring, in: *Landslides in Cold Regions in the Context of Climate Change*, edited by: Shan, W., Guo, Y., Wang, F., Marui, H., and Strom, A., Springer International Publishing, Cham, 177–190, [https://doi.org/10.1007/978-3-319-00867-7\\_13](https://doi.org/10.1007/978-3-319-00867-7_13), 2014.
- Cazzanil, L., Colesanti, C., Leva, D., Nesti, G., Prati, C., Roccal, F., Tarchi, D., and di Milano, P.: A ground based parasitic SAR experiment, *Geoscience and Remote Sensing, IEEE Trans.*, 38, 2132–2141, 2000.
- Colesanti, C. and Wasowski, J.: Investigating landslides with space-borne Synthetic Aperture Radar (SAR) interferometry, *Eng. Geol.*, 88, 173–199, <https://doi.org/10.1016/j.enggeo.2006.09.013>, 2006.
- Dai, K., Deng, J., Xu, Q., Li, Z., Shi, X., Hancock, C., Wen, N., Zhang, L., and Zhuo, G.: Interpretation and sensitivity analysis of the InSAR line of sight displacements in landslide measurements, *GISci. Remote Sens.*, 59, 1226–1242, <https://doi.org/10.1080/15481603.2022.2100054>, 2022.
- Dehls, J., Giudici, D., Farina, P., Martin, D., and Froese, D.: Monitoring Turtle Mountain using ground-based synthetic aperture radar (GB-InSAR), *GeoCalgary, Calgary, AB, Canada*, 1635–1640, [https://members.cgs.ca/documents/conference2010/GEO2010/pdfs/GEO2010\\_218.pdf](https://members.cgs.ca/documents/conference2010/GEO2010/pdfs/GEO2010_218.pdf) (last access: 25 July 2024), 2010.
- Eltner, A. and Sofia, G.: Structure from motion photogrammetric technique, in: *Developments in Earth Surface Processes*,

- vol. 23, Elsevier, 1–24, <https://doi.org/10.1016/B978-0-444-64177-9.00001-1>, 2020.
- Fei, L., Choanji, T., Derron, M.-H., Jaboyedoff, M., Sun, C., and Wolff, C.: Retreat analysis of a sandstone marl interbedded cliff based on a three-year remote sensing survey: A case study at La Cornalle, Switzerland, in: EGU General Assembly 2023, Vienna, Austria, 23–28 April 2023, EGU23-7617, <https://doi.org/10.5194/egusphere-egu23-7617>, 2023.
- Ferretti, A., Monti-Guarnieri, A., Prati, C., Rocca, F., and Massonnet, D.: SAR images of the Earth’s surface, in: InSAR Principles: Guidelines for SAR Interferometry Processing and Interpretation, the Netherlands, 11–38, [https://www.esa.int/About\\_Us/ESA\\_Publications/InSAR\\_Principles\\_Guidelines\\_for\\_SAR\\_Interferometry\\_Processing\\_and\\_Interpretation\\_br\\_ESA\\_TM-19](https://www.esa.int/About_Us/ESA_Publications/InSAR_Principles_Guidelines_for_SAR_Interferometry_Processing_and_Interpretation_br_ESA_TM-19) (last access: 16 December 2022), 2007.
- Ferretti, A., Rucci, A., Tamburini, A., Del Conte, S., and Cespa, S.: Advanced InSAR for Reservoir Geomechanical Analysis, in: EAGE Workshop on Geomechanics in the Oil and Gas Industry, May 2014, Dubai, United Arab Emirates, <https://doi.org/10.3997/2214-4609.20140459>, 2014.
- Fratini, P., Crosta, G. B., Rossini, M., and Allievi, J.: Activity and kinematic behaviour of deep-seated landslides from PS-InSAR displacement rate measurements, *Landslides*, 15, 1053–1070, <https://doi.org/10.1007/s10346-017-0940-6>, 2018.
- Gabriel, A. K., Goldstein, R. M., and Zebker, H. A.: Mapping small elevation changes over large areas: Differential radar interferometry, *J. Geophys. Res.*, 94, 9183, <https://doi.org/10.1029/JB094iB07p09183>, 1989.
- Garthwaite, M. C., Miller, V. L., Saunders, S., Parks, M. M., Hu, G., and Parker, A. L.: A Simplified Approach to Operational InSAR Monitoring of Volcano Deformation in Low- and Middle-Income Countries: Case Study of Rabaul Caldera, Papua New Guinea, *Front. Earth Sci.*, 6, 240, <https://doi.org/10.3389/feart.2018.00240>, 2019.
- Goldstein, R. M., Zebker, H. A., and Werner, C. L.: Satellite radar interferometry: Two-dimensional phase unwrapping, *Radio Sci.*, 23, 713–720, <https://doi.org/10.1029/RS023i004p00713>, 1988.
- Griffiths, H.: Interferometric synthetic aperture radar, *Electron. Commun. Eng. J.*, 7, 247–256, <https://doi.org/10.1049/ecej:19950605>, 1995.
- Hein, A.: Processing of SAR Data: Fundamentals, in: *Signal Processing, Interferometry*, Springer, <https://doi.org/10.1007/978-3-662-09457-0>, 2004.
- Henderson, F. M. and Lewis, A. J.: Radar Fundamentals: The Geoscience Perspective, in: *Principles and Application of Imaging Radar: Manual of Remote Sensing*, John Wiley, New York, 131–181, ISBN 9780471294061, 1998.
- Hilley, G. E., Bürgmann, R., Ferretti, A., Novali, F., and Rocca, F.: Dynamics of Slow-Moving Landslides from Permanent Scatterer Analysis, *Science*, 304, 1952–1955, <https://doi.org/10.1126/science.1098821>, 2004.
- Jaboyedoff, M., Blikra, L., Crosta, G. B., Froese, C., Hermanns, R., Oppikofer, T., Böhme, M., and Stead, D.: Fast assessment of susceptibility of massive rock instabilities, in: *Landslides and Engineered Slopes: Protecting Society through Improved Understanding*, Taylor & Francis Group, London, UK, 459–465, ISBN 978-0-415-62123-6, 2012.
- Jensen, J. R.: chap. 9. Active and Passive Microwave Remote Sensing, in: *Remote Sensing of the Environment: An Earth Resource Perspective*, 2nd Edn., Artech House, ISBN 13:978-0890061923, 2006.
- Klauder, J. R., Price, A. C., Darlington, S., and Albersheim, W. J.: The Theory and Design of Chirp Radars, *Bell Syst. Tech. J.*, 39, 745–808, <https://doi.org/10.1002/j.1538-7305.1960.tb03942.x>, 1960.
- Kropatsch, W. G. and Strobl, D.: The generation of SAR layover and shadow maps from digital elevation models, *IEEE T. Geosci. Remote*, 28, 98–107, <https://doi.org/10.1109/36.45752>, 1990.
- Leva, D., Nico, G., Tarchi, D., Fortuny-Guasch, J., and Sieber, A. J.: Temporal analysis of a landslide by means of a ground-based SAR interferometer, *IEEE T. Geosci. Remote*, 41, 745–752, <https://doi.org/10.1109/TGRS.2003.808902>, 2003.
- Lin, Y.-C. and Fuh, C.-S.: Distortion correction for digital cameras, in: *Proceedings SIBGRAPI’98, International Symposium on Computer Graphics, Image Processing, and Vision*, 20–23 October 1998, Rio de Janeiro, Brazil, 396–401, <https://doi.org/10.1109/SIBGRA.1998.722778>, 1998.
- Lingua, A., Piatti, D., and Rinaudo, F.: Remote Monitoring Of A Landslide Using An Integration Of GB-INSAR And Lidar Techniques, in: *Technical Commission I, XXIst ISPRS Congress*, Beijing, China, 361–366, [https://www.isprs.org/proceedings/XXXVII/congress/1\\_pdf/60.pdf](https://www.isprs.org/proceedings/XXXVII/congress/1_pdf/60.pdf) (last access: 25 July 2024), 2008.
- Lipson, S. G., Lipson, H., and Tannhauser, D. S.: *Waves*, in: *Optical Physics*, The press syndicate of the university of Cambridge, Cambridge, 15–35, ISBN 978-0-521-43047-0, 1995.
- Mahafza, B. R.: *Radar systems analysis and design using Matlab*, Chapman & Hall/CRC, Boca Raton, 529 pp., ISBN 978-1-58488-182-7, 2000.
- Mancini, F., Grassi, F., and Cenni, N.: A Workflow Based on SNAP–StaMPS Open-Source Tools and GNSS Data for PSI-Based Ground Deformation Using Dual-Orbit Sentinel-1 Data: Accuracy Assessment with Error Propagation Analysis, *Remote Sens.*, 13, 753, <https://doi.org/10.3390/rs13040753>, 2021.
- MATLAB: `gradientm`, [https://ch.mathworks.com/help/map/ref/gradientm.html?searchHighlight=gradientm&s\\_tid=srchtitle\\_support\\_results\\_1\\_gradientm](https://ch.mathworks.com/help/map/ref/gradientm.html?searchHighlight=gradientm&s_tid=srchtitle_support_results_1_gradientm) (last access: 2 November 2023), 2023.
- Massonnet, D., Rossi, M., Carmona, C., Adragna, F., Peltzer, G., Feigl, K., and Rabautte, T.: The displacement field of the Landers earthquake mapped by radar interferometry, *Nature*, 364, 138–142, <https://doi.org/10.1038/364138a0>, 1993.
- McCandless, S. and Jackson, C.: Chapter 1. Principles of Synthetic Aperture Radar, in: *Synthetic Aperture Radar Marine User’s Manual*, NOAA, <https://sarusersmanual.com/> (last access: 16 December 2022), 2004.
- Miron, D.: Chapter 2 – Antenna Fundamentals I, in: *Small Antenna Design*, *Small Antenna Design*, 2006, 9–41, <https://doi.org/10.1016/B978-075067861-2/50004-0>, 2006.
- Nadav, L.: Radar, in: *Encyclopedia of Physical Science and Technology*, 3rd Edn., Academic Press, 497–510, ISBN 978-0-12-227410-7, 2003.
- Noferini, L., Pieraccini, M., Mecatti, D., Luzi, G., Atzeni, C., Tamburini, A., and Broccolato, M.: Permanent scatterers analysis for atmospheric correction in ground-based SAR interferometry, *IEEE T. Geosci. Remote*, 43, 1459–1471, <https://doi.org/10.1109/TGRS.2005.848707>, 2005.

- Pedrazzini, A., Jaboyedoff, M., Derron, M.-H., Abellán, A., and Orozco, C. V.: Reinterpretation of displacements and failure mechanisms of the upper portion of Randa rock slide, *Geo-Calgary 2010*, Calgary, AB, Canada, [https://members.cgs.ca/documents/conference2010/GEO2010/pdfs/GEO2010\\_118.pdf](https://members.cgs.ca/documents/conference2010/GEO2010/pdfs/GEO2010_118.pdf) (last access: 14 July 2024), 2010.
- Pieraccini, M. and Miccinesi, L.: Ground-Based Radar Interferometry: A Bibliographic Review, *Remote Sens.*, 11, 1029, <https://doi.org/10.3390/rs11091029>, 2019.
- Pipia, L., Fabregas, X., Aguasca, A., and Lopez-Martinez, C.: Atmospheric Artifact Compensation in Ground-Based DInSAR Applications, *IEEE Geosci. Remote Sens. Lett.*, 5, 88–92, <https://doi.org/10.1109/LGRS.2007.908364>, 2008.
- Rees, W. G.: Technical note: Simple masks for shadowing and highlighting in SAR images, *Int. J. Remote Sens.*, 21, 2145–2152, <https://doi.org/10.1080/01431160050029477>, 2000.
- Rouyet, L., Kristensen, L., Derron, M.-H., Michoud, C., Blikra, L. H., Jaboyedoff, M., and Lauknes, T. R.: Evidence of rock slope breathing using ground-based InSAR, *Geomorphology*, 289, 152–169, <https://doi.org/10.1016/j.geomorph.2016.07.005>, 2017.
- Rudolf, H., Leva, D., Tarchi, D., and Sieber, A. J.: A mobile and versatile SAR system, in: *IEEE 1999 International Geoscience and Remote Sensing Symposium, IGARSS'99*, 28 June–2 July 1999, Hamburg, Germany, 592–594, <https://doi.org/10.1109/IGARSS.1999.773575>, 1999.
- Sabins, F. F.: *Remote Sensing: Principles and Interpretation*, in: 3rd Edn., W. H. Freeman, 494 pp., ISBN 0716724421, 1997.
- Stimson, G. W.: chap. 30. Meeting High Resolution Ground Mapping Requirements, in: *Introduction to Airborne Radar*, vol. PM56, SPIE Press, 393–424, ISBN 1-891121-01-4, 1998.
- Strozzi, T., Antonova, S., Günther, F., Mätzler, E., Vieira, G., Wegmüller, U., Westermann, S., and Bartsch, A.: Sentinel-1 SAR Interferometry for Surface Deformation Monitoring in Low-Land Permafrost Areas, *Remote Sens.*, 10, 1360, <https://doi.org/10.3390/rs10091360>, 2018.
- Sturzenegger, M., Yan, M., Stead, D., and Elmo, D.: Application and limitations of ground-based laser scanning in rock slope characterization, in: *Rock Mechanics: Meeting Society's Challenges and Demands*, edited by: Eberhardt, E., Stead, D., and Morrison, T., Taylor & Francis, 29–36, ISBN 978-0-415-44401-9, ISBN 978-1-4398-5657-4, 2007.
- Talich, M.: The Deformation Monitoring of Dams by the Ground-Based InSAR Technique – Case Study of Concrete Hydropower Dam Orlik, *Int. J. Adv. Agricult. Environ. Eng.*, 3, 192–197, <https://doi.org/10.15242/IJAAEE.A0416051>, 2016.
- Tapete, D., Casagli, N., Luzi, G., Fanti, R., Gigli, G., and Leva, D.: Integrating radar and laser-based remote sensing techniques for monitoring structural deformation of archaeological monuments, *J. Archaeolog. Sci.*, 40, 176–189, <https://doi.org/10.1016/j.jas.2012.07.024>, 2013.
- Tarchi, D.: Monitoring landslide displacements by using ground-based synthetic aperture radar interferometry: Application to the Ruinon landslide in the Italian Alps, *J. Geophys. Res.*, 108, 2387, <https://doi.org/10.1029/2002JB002204>, 2003.
- Tarchi, D., Ohlmer, E., and Sieber, A.: Monitoring of Structural Changes by Radar Interferometry, *Res. Nondestruct. Eval.*, 9, 213–225, <https://doi.org/10.1080/09349849709414475>, 1997.
- Toomay, J. C. and Hannen, P. J.: *Radar Principles for the Non-specialist*, in: 3rd Edn., Scitech Publishing, ISBN 978-1-891121-28-9, 2004.
- Turner, I. L., Harley, M. D., Almar, R., and Bergsma, E. W. J.: Satellite optical imagery in Coastal Engineering, *Coast. Eng.*, 167, 103919, <https://doi.org/10.1016/j.coastaleng.2021.103919>, 2021.
- Usai, S. and Hanssen, R.: Long time scale INSAR by means of high coherence features, in: *Proc. Ers. Symposium*, 414 pp., <https://repository.tudelft.nl/record/uuid:d1df5565-3451-4d9e-a219-7c15549cba43> (last access: 25 July 2024), 1997.
- Werner, C., Strozzi, T., Wiesmann, A., and Wegmüller, U.: A real aperture radar for ground-based differential interferometry, in: *Proc. IGARSS*, 7–11 July 2008, Boston, MA, 1–2, <https://doi.org/10.1109/IGARSS.2008.4779320>, 2008.
- Wicks, C., Thatcher, W., and Dzurisin, D.: Migration of Fluids Beneath Yellowstone Caldera Inferred from Satellite Radar Interferometry, *Science*, 282, 458–462, <https://doi.org/10.1126/science.282.5388.458>, 1998.
- Wolberg, J.: Chapter 2: The method of Least Squares, in: *Data Analysis Using the Method of Least Squares: Extracting the Most Information from Experiments*, Germany, Springer, Berlin, Heidelberg, 31–49, ISBN 3-540-25674-1, 2006.
- Wolff, C.: Frequency-Modulated Continuous-Wave Radar (FMCW Radar): <https://www.radartutorial.eu/> (last access: 25 April 2023), 1998.
- Wolff, C.: charlottewolff/GB-PAR: first (first), Zenodo [code], <https://doi.org/10.5281/zenodo.12820384>, 2024.
- Wolff, C., Jaboyedoff, M., Fei, L., Pedrazzini, A., Derron, M.-H., Rivolta, C., and Merrien-Soukatchoff, V.: Assessing the Hazard of Deep-Seated Rock Slope Instability through the Description of Potential Failure Scenarios, Cross-Validated Using Several Remote Sensing and Monitoring Techniques, *Remote Sens.*, 15, nb:5396, <https://doi.org/10.3390/rs15225396>, 2023.
- Woodhouse, I. H.: chap. 10. Imaging Radar, in: *Introduction to Microwave Remote Sensing*, CRC Press, 45 pp., ISBN 978-1-315-27257-3, 2006.
- Zebker, H. A. and Villasenor, J.: Decorrelation in interferometric radar echoes, *IEEE T. Geosci. Remote*, 30, 950–959, <https://doi.org/10.1109/36.175330>, 1992.